Encontreitor: First Radiants

Leonardo S. Amaral[1,2], *Carlos A.P.B. Bella*[1], *Lauriston S. Trindade*[1], *Gabriel G. Silva*[1,3], *Rubens Damigle*[1], *Marcelo L.P.V. Zurita*[1], *Marcelo W.S. Domingues*[1], *Renato C. Poltronieri*[1], *Cristóvão J.L. Faria*[1,4], *Carlos F. Jung*[1,4]

This article presents the results of a new method implemented in the Encontreitor software (Amaral et al., 2018b). Twenty-three new radiants were found at first with this computational application. The software input is a set of meteor orbits extracted from databases from meteor video-monitoring networks, such as BRAMON (Amaral et al., 2018a), EDMOND (Kornoš et al., 2014a; Kornoš et al., 2014b; EDMOND, 2018) and SonotaCo (SonotaCo, 2009; SonotaCo, 2018), after applying the five steps of the method, the application provides a list of possible new radiants.

Received 2019 December 5

1 Introduction

The Encontreitor software was developed using the Visual Basic programming language and it implements features that allow it to execute the five steps described in the method proposed by Amaral et al. (2018a). The tool implements the calculation of the Drummond determinant D describing the orbital dissimilarity (Drummond, 1981; Galligan, 2001; Jopek et al., 2002). This also implements the Break-point+, Valideitor and Lapdeitor methods (Amaral et al., 2018b). This software was used to discover the 23 radiants described in this article, in addition to being responsible for the tabulation of the data used to create the plots (see the interface shown in Figure 1).

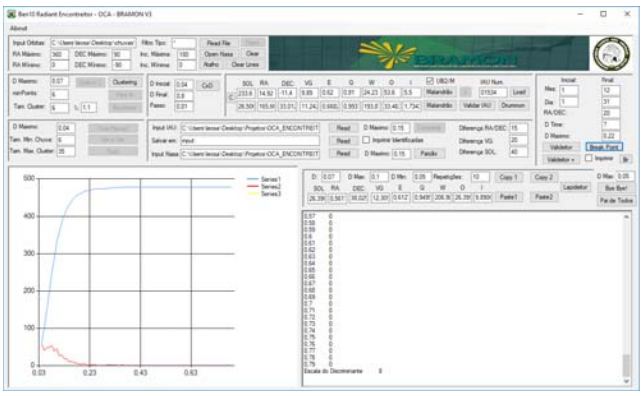

Figure 1 – Graphic Interface of the Encontreitor Software (Amaral et al., 2018b).

[1]BRAMON – Brazilian Meteor Observation Network, Nhandeara, Brazil
Email: carlos.pbella@gmail.com; lauristontrindade@yahoo.com.br; rubens.marreira@gmail.com; marcelozurita@gmail.com; marcelo@casb.com.br; rcpoltronieri@gmail.com
[2]OCA – Observatório Campo dos Amarais, Bilac, Brazil (MPC X74). Email: lsamaral-ios@hotmail.com
[3]Instituto de Química, Universidade de São Paulo, São Paulo, Brazil. Email: gabrielg@iq.usp.br
[4]SONEAR – Southern Observatory for Near Earth Asteroids, Oliveira, Brazil (MPC Y00). Email: cjacqueslf@gmail.com
[5]HELLER & JUNG – Space and Sky Observatory, Taquara, Brazil. Email: carlosfernandojung@gmail.com

IMO bibcode WGN-483-amaral-radiants
NASA-ADS bibcode 2020JIMO...48...69A

2 Reporting Radiants to the IAU

From May 2017 to January 2018, six reports of new radiants were sent to the IAU (International Astronomical Union) totalling 121 new radiants. These new radiants were found using the Encontreitor software and databases from the BRAMON, SonotaCo and EDMOND networks. This article presents the first 23 radiants found, as listed in Table 1. The three-letter codes as well as the designation of the showers are assigned by the IAU MDC.

The mean orbit generated by each radiant (see Table 1) has a low D value (always below 0.07) with respect to the meteors used to find each radiant. As described in Amaral et al. (2018a), the values listed in Table 1 comprise the radiant's nucleus and were used to generate the mean orbit.

Later in the paper we describe each of the 23 new radiants in detail. The results of the analysis are presented as a three-parameter plot (right ascension α – declination δ – geocentric velocity V_g) of the distribution of the orbits for each radiant. These plots were built from a search in the meteor orbit databases BRAMON, EDMOND, and SonotaCo, looking for orbits that are similar ($D \leq 0.22$) to the mean orbits associated to the meteors of the radiants. Breakpoint+ and Valideitor plots are also be presented. Details on how these methods work and explanations of the graphs can be found in (Amaral et al., 2018b). These plots allow us to understand how meteors defining a radiant are related to meteors of other radiants.

All radiants described have been tested against all radiants in the current IAU database in order to ensure that they have a high orbital distance to other existing radiants.

3 Radiants

3.1 NEC – November Cetids

Before Encontreitor was created, two radiants were found by BRAMON using visual data (described by Trindade et al., 2019). The NEC radiant was also visually identified and later detected by Encontreitor. Initially, in the search for this radiant, only the BRAMON orbit database was used. The NEC radiant marks a change in the methodology used by BRAMON in the search for new radiants.

Table 1 – New radiants found in this study. Number – number of orbits; parent – possible parent object.

Code	Name	$\lambda_\odot$	α	δ	$\Delta\alpha$	$\Delta\delta$	V_G	a	q	e	ω	Ω	i	Number	Parent
NEC	November Cetids	233.6	14.92	−11.4	0.3	−0.3	9.89	2.39	0.91	0.62	24.23	53.6	5.5	265	2016 BE_1, 2014 DS_{22}, 2007 TW_{24}, and 2014 UA_8?
JCT	July Cetids	110.4	19.48	−7.7	0.9	0.5	66.2	3.67	0.99	0.73	20.0	290.0	153.7	28	
JCD	June Cetids	88.7	20.13	−23.23	1.3	0	62.52	10.22	0.92	0.91	330.05	268.71	128.46	7	
ADS	June Aquariids	91.7	333.6	−18.46	1.0	0.4	60.89	2.44	0.44	0.82	115.53	271.68	160.02	11	
LSA	Lambda Sagitariids	74.2	276.85	−24.76	0.6	0.1	35.15	2.00	0.16	0.92	138.8	254.23	6.06	77	
DGR	Delta2 Gruids	91.3	339.09	−43.41	0.0	0.0	53.12	6.50	0.52	0.92	91.66	271.29	102.14	6	
GSC	Gamma Sculptorids	86.6	348.21	−28.42	0.7	0.5	63.54	7.00	0.77	0.89	60.33	266.55	138.45	13	
SGI	June Sagittariids	72.8	277.58	−20.37	0.6	0.0	37.51	2.40	0.12	0.95	324.13	72.84	4.88	32	
FLO	February Leonids	329.6	166.57	4.13	0.6	−0.2	32.44	2.17	0.26	0.88	125.51	149.57	4.06	79	
PCS	Phi Capricornids	226.9	318.09	−19.26	−0.2	0.4	7.06	1.85	0.98	0.47	349.43	46.9	3.12	44	2009 WX_7, 2010 VW_{194}, 2014 WX_4, 2015 XM_{169}?
USG	Phi Ophiuchids	50.7	251.03	−17.46	0.4	−0.04	35.73	2.43	0.17	0.93	317.06	50.74	6.78	67	
XCD	October Cetids	187.5	37.99	7.67	0.2	0.3	39.75	1.75	0.07	0.96	152.6	7.46	27.4	29	
LCP	Lambda Capricornids	202.1	326.12	−11.74	0.6	0.0	6.37	1.72	0.98	0.43	13.76	22.15	2.63	41	2014 RQ_{17}, 2016 TD_{11}?
NAA	November alpha Aurigids	231.38	80.64	47.24	0.1	0.0	45.05	5.50	0.22	0.96	304.45	231.38	65.12	39	
OAC	October alpha Camelopardalids	213.6	56.47	64.46	0.9	0.1	43.37	7.38	0.59	0.92	261.05	213.63	69.8	38	
CVD	January Canum Venaticids	304.4	185.86	40.48	0.0	0.0	47.37	6.50	0.52	0.92	269.19	304.43	79.28	43	
CVT	February Canum Venaticids	331.8	195.72	36.09	0.0	0.0	39.96	6.38	0.51	0.92	269.96	331.8	56.5	45	
PCI	42 Piscids	135.6	7.1	12.44	0.5	0.3	59.72	5.40	0.27	0.95	300.51	135.65	155.74	31	
OAG	October Aurigids	205.0	70.24	35.53	0.4	0.1	56.19	5.33	0.16	0.97	314.16	205.04	130.65	31	
SPS	Sigma Perseids	182.3	51.51	47.38	0.0	−0.1	55.37	3.00	0.51	0.83	274.85	182.29	115.54	32	
TRD	October Taurids	192.4	69.81	12.46	0.6	0.0	60.9	6.20	0.31	0.95	114.59	12.45	153.49	37	
DRP	December rho Puppids	251.2	124.4	−24.2	0.4	−0.1	53.67	8.78	0.79	0.91	54.41	71.23	97.11	26	

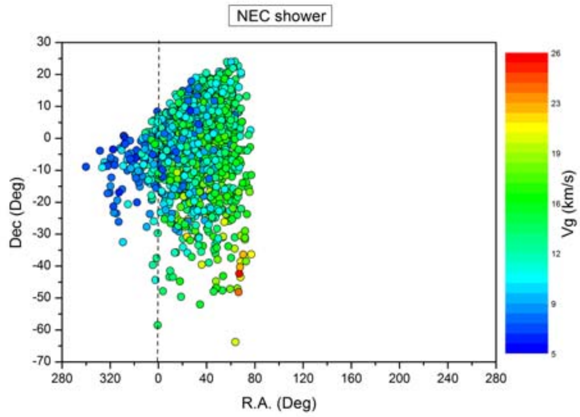

Figure 2 – Radiant of the November Cetids (NEC).

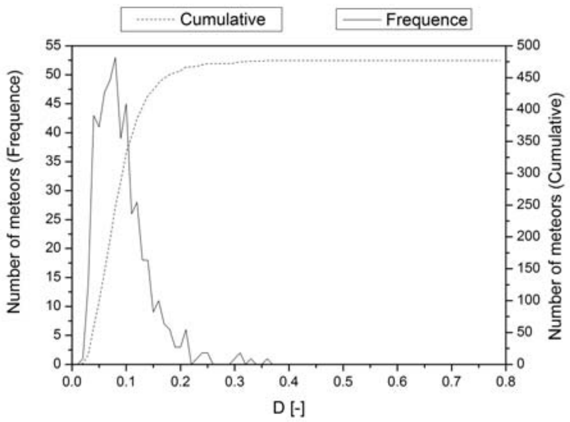

Figure 3 – NEC Break-point+ with a 20 degree radius.

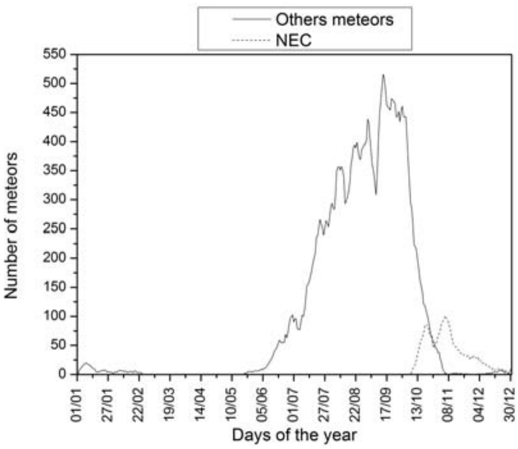

Figure 4 – NEC Valideitor, 20° radius ($D \leq 0.22$).

Figure 2 presents the NEC radiant orbit distribution. It shows that the radiants cover a large area of the sky (right ascension from $\approx 300°$ to $\approx 70°$ and declination from $\approx -50°$ to $\approx +25°$). Further, we see an apparent velocity increase as the rights ascension increases and the declination decreases.

Figure 3 shows the NEC breakpoint+ plot, in which we can see that the plot's inflection point occurs very early, close to $D = 0.15$. This means that, despite being a radiant with few orbits recorded by now, they are well concentrated relative to the mean orbit found for meteors of this radiant (hereafter we use the shorter "radiant's mean orbit").

Figure 4 presents the Valideitor plot (Amaral et al., 2018b). It shows the distribution of the orbits associated to the radiant as a function of the dates the meteors were captured. Only meteors within a radius of 20° around the radiant's center are considered. The continuous line represents meteors not belonging to the radiant ($D > 0.22$), and the dotted line represents meteors belonging to the radiant ($D \leq 0.22$).

In this graph we can identify the formation of two maximum-activity peaks in the radiant. We also note the intense activity of meteors which do not belong to the NEC radiant, but which are probably associated to other radiants. At the time of the second peak, there is essentially no activity from other radiants in the area defined by Valideitor, which allowed the detection of the radiant in visual data. It is important to notice that for several months of the year, this region of the sky was only visible during the day, therefore no meteors were captured during this period.

Despite the high activity of other meteors not belonging to the radiant, these meteors are distant from NEC in terms of their orbits. This becomes clear when we compare the numbers from the breakpoint+ and Valideitor plots. In the breakpoint plot, the maximum number of meteors reached by NEC is about 475. Even if we increase the D value up to 0.8, the number of meteors does not increase significantly after $D = 0.2$. But when we look at the Valideitor plot, it becomes evident that in the 20° radius area used to create the plots (breakpoint+ and Valideitor) there were many other meteors besides these roughly 475 (the total number of meteors was 5783).

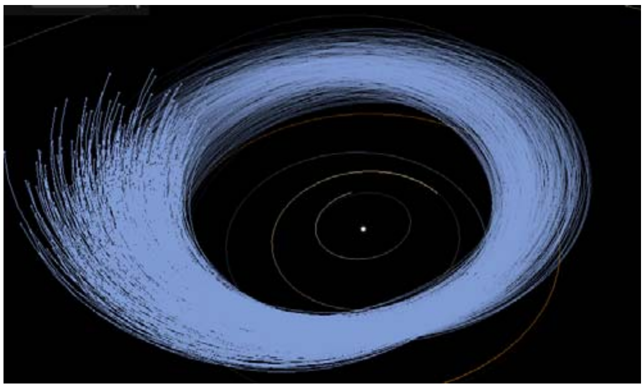

Figure 5 – Stream representation of the NEC ($D \leq 0.1$).

Figure 5 is a simple stream representation of the meteoroids associated to the NEC radiant. The purpose of the figure is just to demonstrate the orbital similarity of the meteoroids which are considered to belong to the radiant. This representation was created by exporting the orbital data of 549 NEC meteors (with $D \leq 0.1$) to the Universe Sandbox (2018) software.

A search for parent bodies of the NEC radiant has returned several possible candidates. The four candidates with the most compatible orbits are 2016 BE_1, 2014 DS_{22}, 2007 TW_{24}, and 2014 UA_8. Of these, 2016 BE_1 is the object with the highest orbital similarity ($D = 0.019$).

A second concentration of NEC meteors (Table 2) that appears to be related to this radiant was also found. This second stream appears to be slightly larger than the first one found. The two groups vary mainly in terms of the parameters ω and Ω. This second stream was found using the BRAMON, SonotaCo, and EDMOND databases, and may indicate that the radiant can be associated to more than one parent body.

Table 2 – Second NEC flow (established from 262 orbits).

$\Delta\alpha$	$\Delta\delta$	$\lambda_\odot$	α	δ	V_G
0°.48	0°.07	219°.8	13°.83	−2°.96	11.92 km/s
a	q	e	ω	Ω	i
2.38 au	0.62 au	0.89	40°.45	39°.8	4°.51

3.2 JCT – July Cetids

Figure 6 shows a plot of the JCT Radiant orbit distribution. The radiant coverage area (right ascension from ≈ 340° to ≈ 50° and declination from ≈ −30° to ≈ +20°) is noteworthy, in addition to an apparent speed increase as the right ascension decreases and the declination increases.

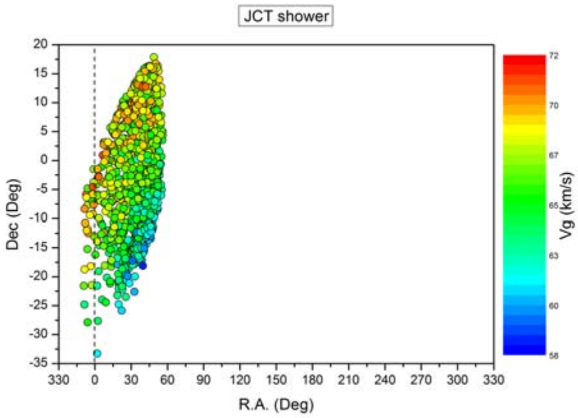

Figure 6 – Radiant of the July Cetids (JCT).

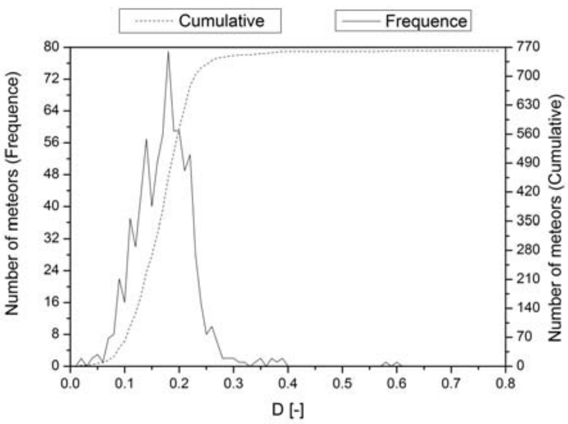

Figure 7 – JCT Break-point+ with a 20 degree radius.

Figure 7 shows the JCT breakpoint+ plot, in which we can see that the plot's inflection point occurs very early, close to $D = 0.22$, i.e., despite being a radiant with few orbits recorded by now, they are well concentrated relative to the radiant's mean orbit.

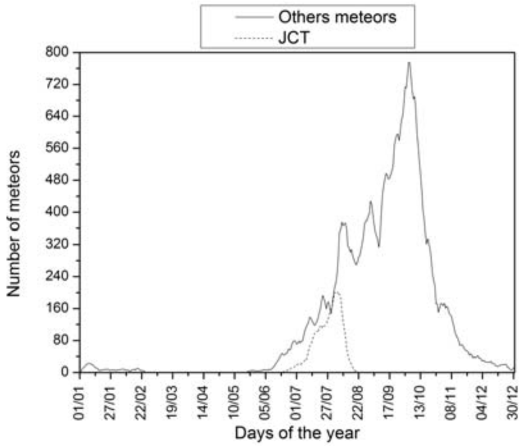

Figure 8 – JCT Valideitor, 20° radius ($D \le 0.22$).

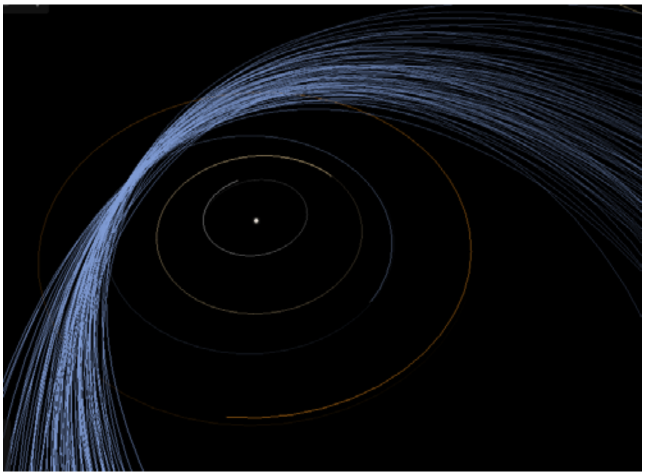

Figure 9 – Stream representation of the JCT ($D \le 0.1$).

Figure 8 presents the Valideitor plot (Amaral et al., 2018b), in which we can identify the formation of a maximum-activity peak in the radiant near the end of July and beginning of August. As detailed for the NEC radiant, we can also see the activity of other radiants along with the JCT radiant, however, according to the breakpoint+ plot, these radiants are orbitally distant from the JCT radiant.

Figure 9 is a stream representation of meteors associated to the JCT radiant. This representation was created by exporting the orbital data of 89 meteors belonging to JCT (with $D \le 0.1$).

3.3 JCD – June Cetids

Figure 10 shows a plot of the JCD radiant orbit distribution, in which we can see the radiant coverage area (right ascension from ≈ 340° to ≈ 50° and declination from ≈ −35° to ≈ −2.5°). Further, we find an apparent speed increase as the right ascension decreases and the declination increases.

Figure 11 shows the breakpoint+ plot for the JCD. We can see that the plot's inflection point occurs close to $D = 0.22$, i.e., despite being a radiant with rather few orbits recorded, they are well concentrated relative to the radiant's mean orbit.

Figure 12 shows the Valideitor plot, in which we can identify that activity from the radiant occurs between the end of June and the middle of August. We can

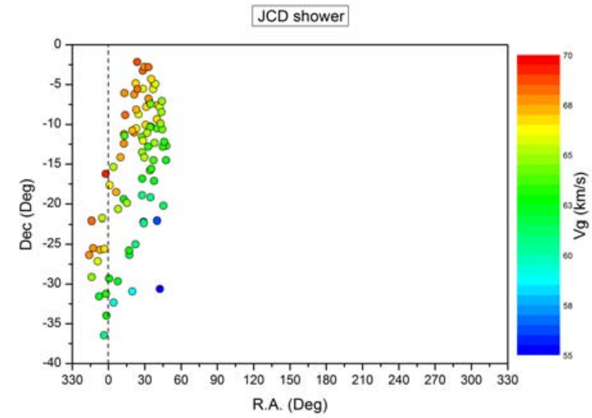

Figure 10 – Radiant of the June Cetids (JCD).

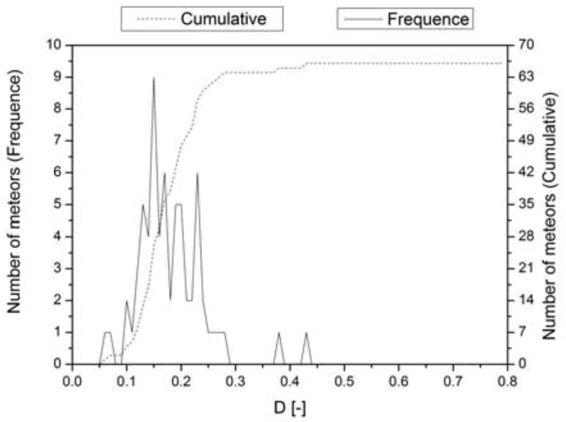

Figure 11 – JCD Break-point+ with a 20 degree radius.

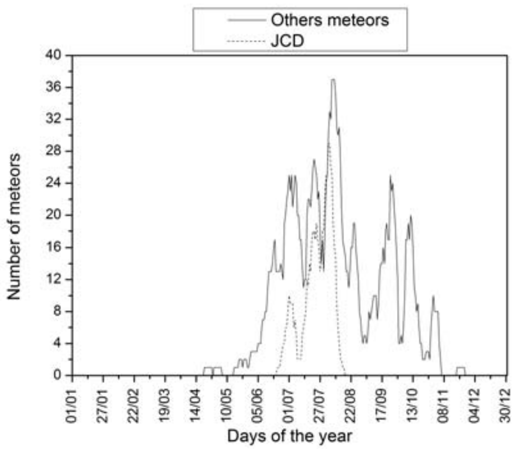

Figure 12 – JCD Valideitor, 20° radius ($D \le 0.22$).

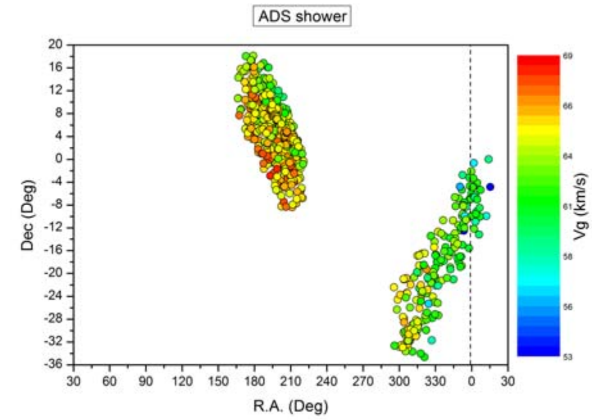

Figure 13 – Radiant of the June Aquariids (ADS).

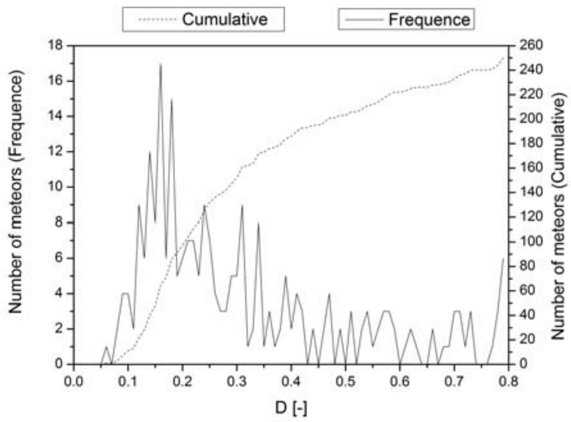

Figure 14 – ADS Break-point+ with a 20 degree radius.

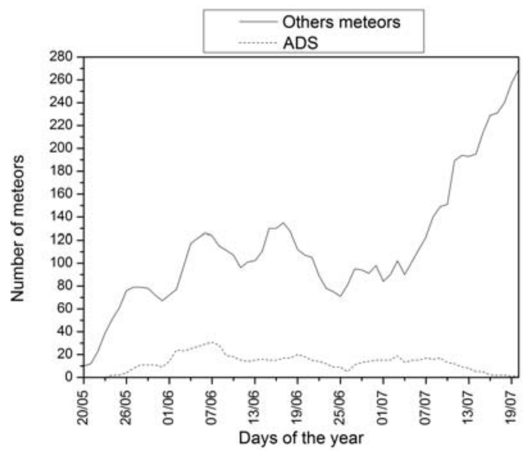

Figure 15 – ADS Valideitor, 20° radius ($D \le 0.22$).

also notice the activity of other radiants along the JCD. As described for the NEC radiant, these other radiants appear to be orbitally distant to the JCD.

3.4 ADS – June Aquariids

Figure 13 shows a plot of the ADS radiant orbit distribution and the radiant coverage area (right ascension from $\approx 290°$ to $\approx 15°$ and declination from $\approx -34°$ to $\approx 0°$). We note that two regions of meteor occurrence are formed. This is because the radiant's orbit crosses the Earth's orbit at two different times, thus generating two radiants. ADS gives rise to the orbit concentration seen to the right, and another radiant (which appears to be 428 DSV – December sigma Virginids) gives rise to the orbit concentration seen to the left. These two radiants may be related and may share a common parent body. We can also note that the speed of the meteors seems to increase as the right ascension decreases and the declination increases.

Figure 14 shows the ADS breakpoint+ plot, and although it starts to "decelerate" around $D = 0.3$, it is not clear where the inflection point is. This means that the orbits are not as strongly concentrated near the mean orbit associated with the radiant. While the mean orbit represents the point of highest concentration of orbits, the orbits associated to the radiant are not all close to

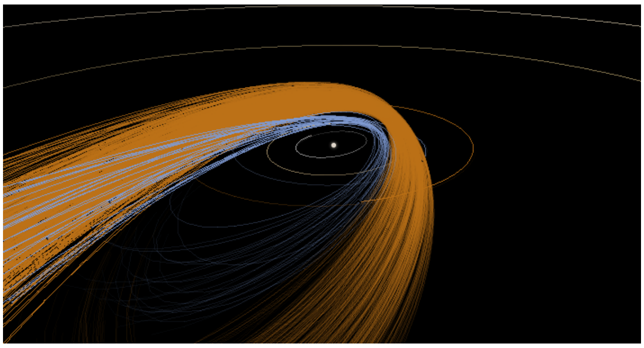

Figure 16 – Stream representation of the ADS and DSV ($D \leq 0.1$).

this center (as we saw in the case of NEC, JCT, and JCD). This could indicate, for example, that this is a radiant with meteoroid orbits which are already "dissipating" (perhaps due to minor orbital changes taking place over time), or even that the ADS could have been formed by several parent bodies with similar orbits.

Figure 15 shows the Valideitor plot, in which we can identify the radiant's activity between the end of May and the middle of July. We can also notice a strong activity of other radiants together with the ADS radiant.

Figure 16 is a stream representation of the meteors of the ADS (in blue) and the DSV (in orange). This representation was created by exporting the orbital data of 28 meteors belonging to the ADS (with $D \leq 0.1$) and 546 from the DSV.

3.5 LSA – Lambda Sagitariids

Figure 17 shows a plot of the JCD radiant orbit distribution, in which we can see the radiant coverage area (right ascension from $\approx 235°$ to $\approx 320°$ and declination from $\approx -34°$ to $\approx -14°$), in addition to an apparent speed increase as the right ascension decreases.

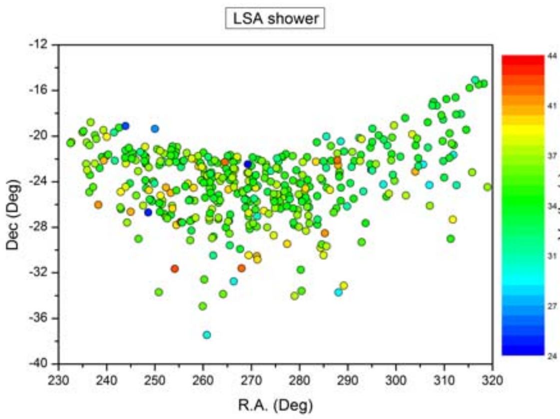

Figure 17 – Radiant of the Lambda Sagitariids (LSA).

Figure 18 shows the LSA breakpoint+ plot, in which the inflection point is late, i.e., the orbits are not strongly concentrated near the radiant's mean orbit.

Figure 19 shows the Valideitor plot, in which we can identify the radiant's peak activity between the middle of May and beginning of June. We can also notice the activity of other radiants along with the LSA radiant. A relationship between the LSA and nearby radiants

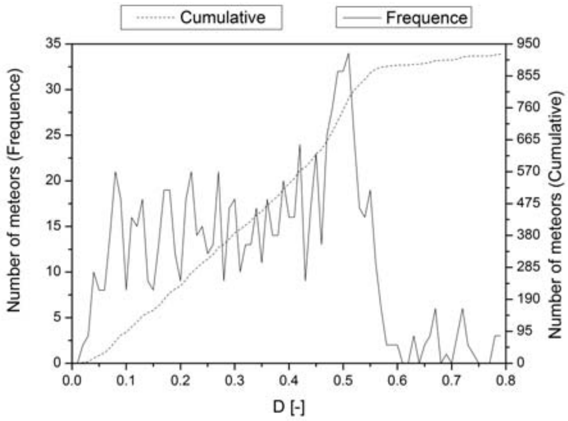

Figure 18 – LSA Break-point+ with a 20 degree radius.

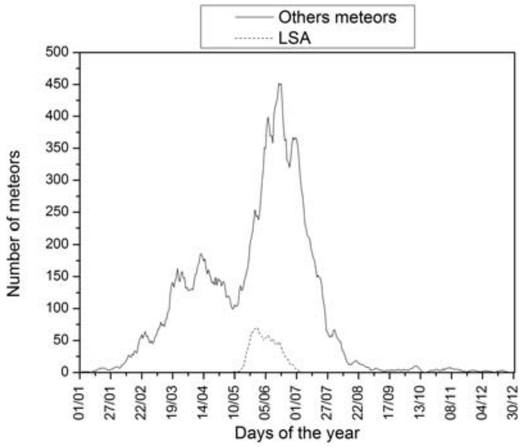

Figure 19 – LSA Valideitor, 20° radius ($D \leq 0.22$).

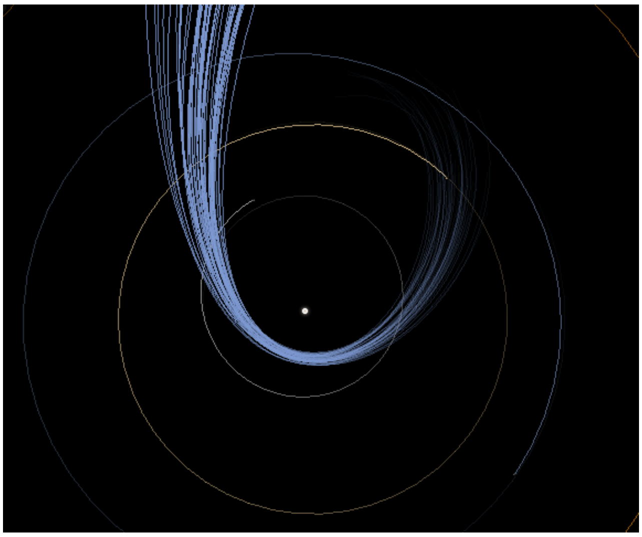

Figure 20 – Stream representation of the LSA ($D \leq 0.07$).

is likely, even though the LSA center is far from other radiants.

Figure 20 is a stream representation of the LSA radiant meteors. This representation was created by exporting the orbital data of 52 meteor belonging to LSA (with $D \leq 0.07$).

3.6 DGR – Delta2 Gruids

Figure 21 shows the orbit distribution of the DGR radiant, and we find the radiant coverage area in right

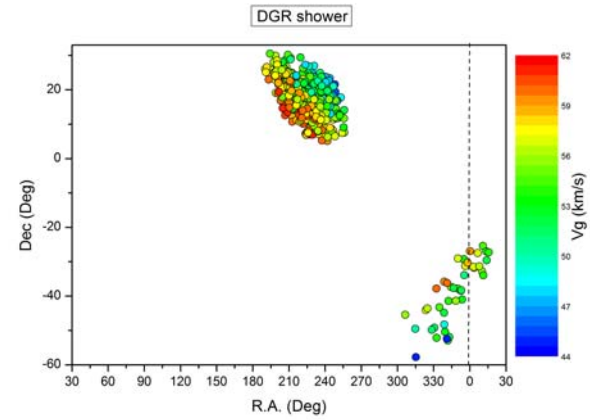

Figure 21 – Radiant of the Delta2 Gruids (DGR).

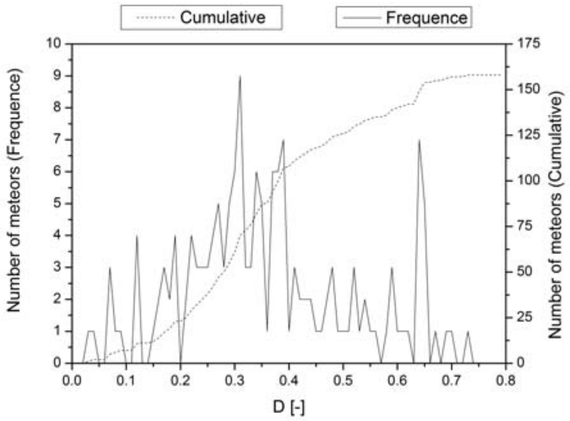

Figure 22 – DGR Break-point+ with a 20 degree radius.

Figure 23 – DGR Valideitor, 20° radius ($D \leq 0.22$).

ascension from $\approx 315°$ to $\approx 15°$ and in declination from $\approx -55°$ to $\approx -22°$. DGR has a twin radiant, while DGR gives rise to the concentration of orbits on the right, another radiant (which appears to be 727 ISR – iota Serpentids) gives rise to the concentration of orbits on the left. These two radiants may be related and share a parent body. We can also notice that the speed of the meteors seems to increase as the right ascension and the declination increases.

Figure 22 shows the DGR breakpoint+ plot, and although it begins to "decelerate" near $D = 0.35$, it is not clear where the inflection point is, i.e., the orbits

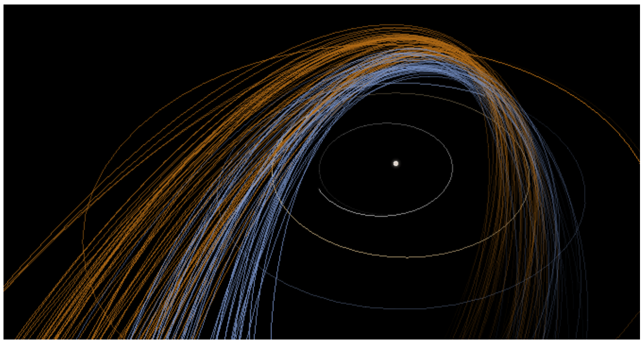

Figure 24 – Stream representation of the DGR and DSV ($D \leq 0.1$).

are not strongly concentrated near the radiant's mean orbit.

Figure 23 shows the Valideitor plot, in which we can identify the radiant's activity occurring between the beginning of June and the middle of July. We can also notice the activity of other radiants occurring together with the DGR radiant. A relationship between the DGR and nearby radiants is possible, even though the DGR center is far from other radiants.

Figure 24 is a stream representation of the DGR (in blue) and ISR (in orange) radiant meteors. This representation was created by exporting the orbital data of 51 meteor belonging to DGR (with $D \leq 0.1$) and 66 from ISR.

3.7 GSC – Gamma Sculptorids

Figure 25 shows the orbit distribution of the GSC radiant, and we can notice the radiant coverage area (right ascension from $\approx 315°$ to $\approx 30°$ and declination from $\approx -45°$ to $\approx -2.5°$). GSC gives rise to orbit concentration on the right, and its twin radiant (not yet published) gives rise to the orbit concentration on the left. These two radiants may be related and share a common parent body. We can also notice that the speed of the meteors seems to increase as the right ascension decreases and the declination increases.

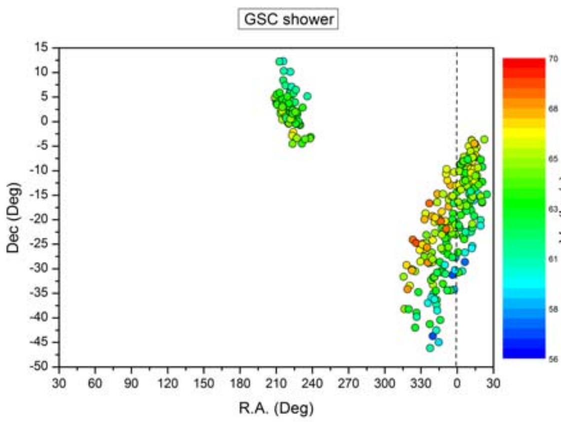

Figure 25 – Radiant of the Gamma Sculptorids (GSC).

Figure 26 presents the GSC breakpoint+ plot, whose inflection point is close to $D = 0.27$.

Figure 27 shows the Valideitor plot, in which we can identify the radiant's activity near the end of May

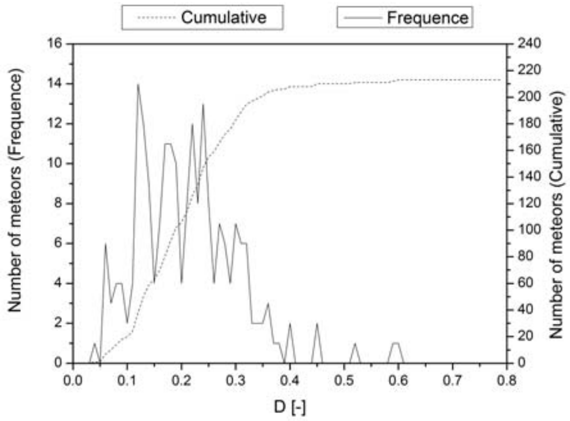

Figure 26 – GSC Breakpoint+ plot with a 20 degree radius.

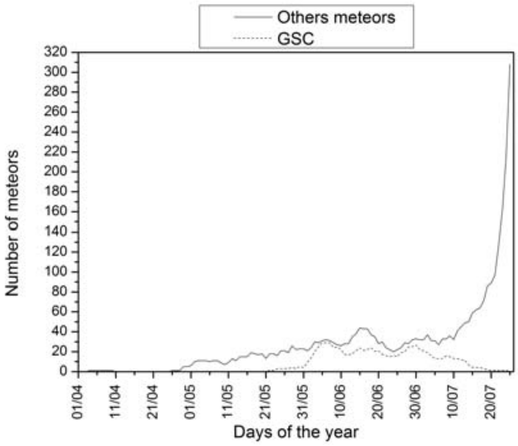

Figure 27 – GSC Valideitor, 20° radius ($D \leq 0.22$).

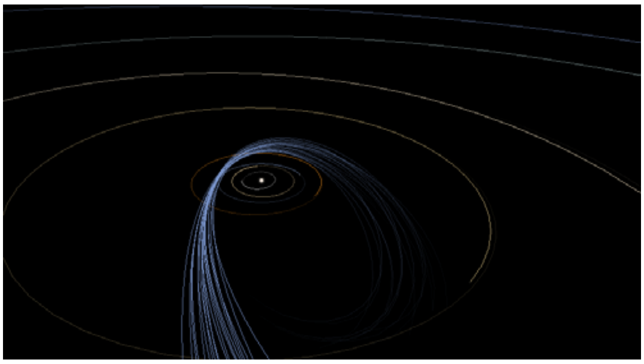

Figure 28 – Stream representation of the GSC ($D \leq 0.1$).

and end of July. We can also notice the activity of other radiants occurring together with the GSC radiant (with a large peak occurring at the end of July).

Figure 28 is a stream representation of the meteors classified as GSC. This representation was created by exporting the orbital data of 20 meteors belonging to the GSC (with $D \leq 0.1$).

3.8 SGI – June Sagittariids

Figure 29 shows the orbit distribution of the DGR radiant, and we can notice the radiant coverage area (right ascension from $\approx 235°$ to $\approx 315°$ and declination from $\approx -22°$ to $\approx -7°$). We can also notice that the speed of the meteors seems to increase as the right ascension decreases and the declination increases.

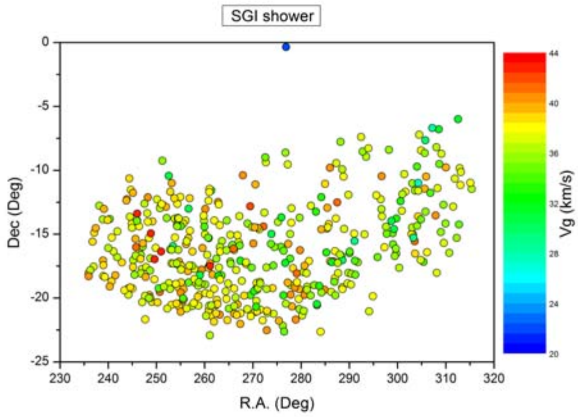

Figure 29 – Radiant of the June Sagittariids (SGI).

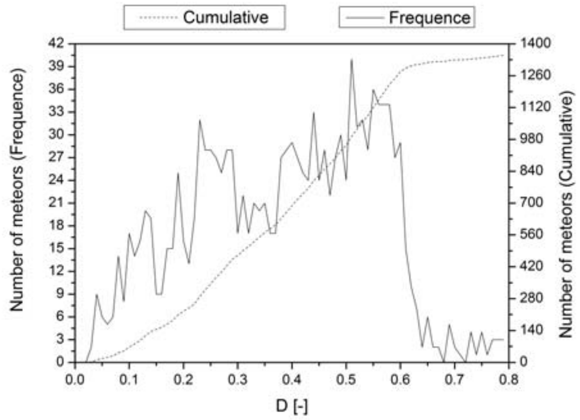

Figure 30 – SGI Breakpoint+ plot with a 20 degree radius.

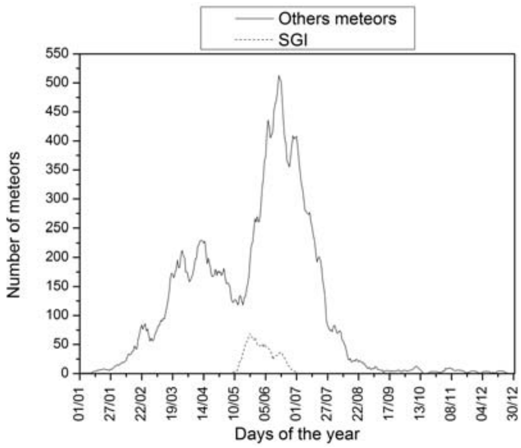

Figure 31 – SGI Valideitor, 20° radius ($D \leq 0.22$).

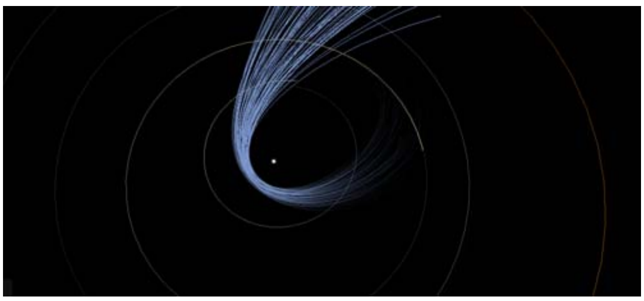

Figure 32 – Stream representation of the SGI ($D \leq 0.1$).

Figure 30 presents the SGI breakpoint+ plot, whose inflection point occurs late, close to $D = 0.6$, i.e., the radiant's orbits are not concentrated in relation to the radiant's mean orbit.

Figure 31 shows the Valideitor plot, in which we can identify the radiant's activity occurring between the middle of May and the beginning of July. We can also notice the activity of other radiants along the SGI radiant. A relationship between the SGI and nearby radiants is likely, even though the SGI center is far from other radiants.

Figure 32 is a stream representation of the SGI radiant meteors. This representation was created by exporting the orbital data of 79 meteor belonging to the SGI (with $D \leq 0.1$).

3.9 FLO – February Leonids

Figure 33 shows the orbit distribution of the FLO radiant, and we can notice the radiant coverage area (right ascension from $\approx 130°$ to $\approx 205°$ and declination from $\approx -17°$ to $\approx +18°$). We can also notice that the speed of the meteors seems to increase as the right ascension decreases and the declination increases.

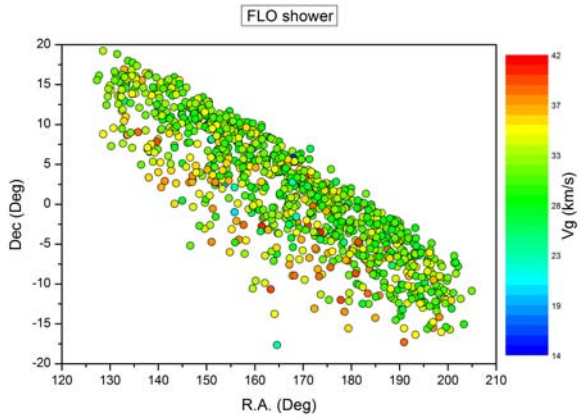

Figure 33 – Radiant of the February Leonids (FLO).

Figure 34 shows the FLO breakpoint+ plot, whose inflection point occurs late, close to $D = 0.4$, i.e., the radiant's orbits are weakly concentrated in relation to the radiant's mean orbit.

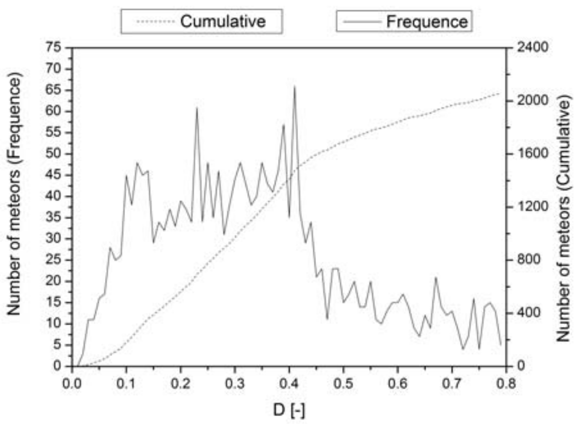

Figure 34 – FLO Breakpoint+ plot with a 20 degree radius.

Figure 35 shows the Valideitor plot, in which we can identify the formation of three maximum activity peaks in the radiant between the middle of July and August, and also the activity of other radiants along with the FLO radiant. The FLO is likely related with nearby radiants.

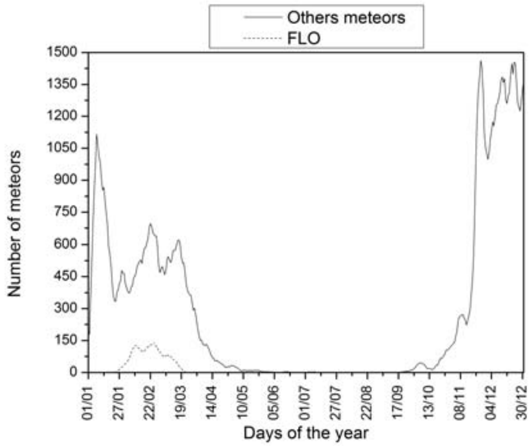

Figure 35 – FLO Valideitor, 20° radius ($D \leq 0.22$).

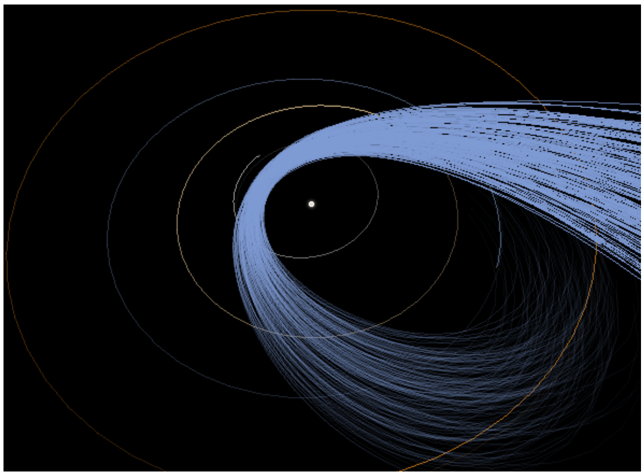

Figure 36 – Stream representation of the FLO ($D \leq 0.1$).

Figure 36 is a streams representation of the FLO radiant meteors. This representation was created by exporting the orbital data of 207 meteors belonging to FLO (with $D \leq 0.1$).

3.10 PCS – Phi Capricornids

Figure 37 shows the orbit distribution of the PCS radiant, and we can notice the radiant coverage area (right ascension from $\approx 270°$ to $\approx 30°$ and declination from $\approx -45°$ to $\approx +5°$). We can also notice that the speed of the meteors seems to increase as the right ascension decreases and the declination increases.

Figure 38 shows the PCS breakpoint+ plot, whose inflection point occurs early, close to $D = 0.2$, i.e., despite being a radiant with few orbits recorded, they are concentrated relative to the mean orbit associated with the radiant.

Figure 39 shows the Valideitor plot, in which we can identify the radiant's activity between the beginning of November and the middle of December. Some of these peaks show a higher occurrence of meteors among radiants that occur in the same period. We can also notice the activity of other radiants along the PCS radiant,

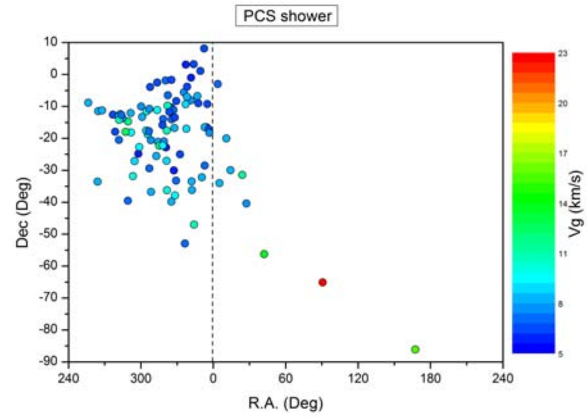

Figure 37 – Radiant of the Phi Capricornids (PCS).

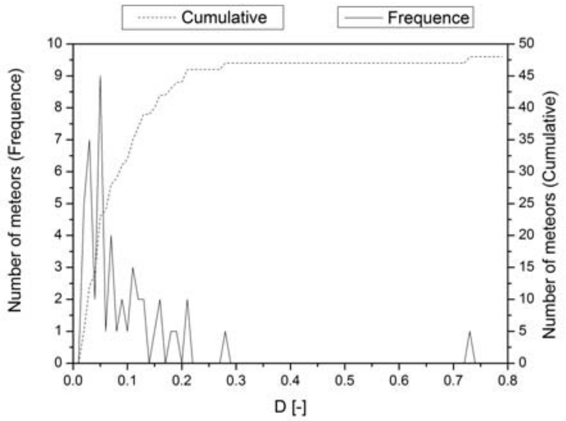

Figure 38 – PCS Breakpoint+ plot with a 20 degree radius.

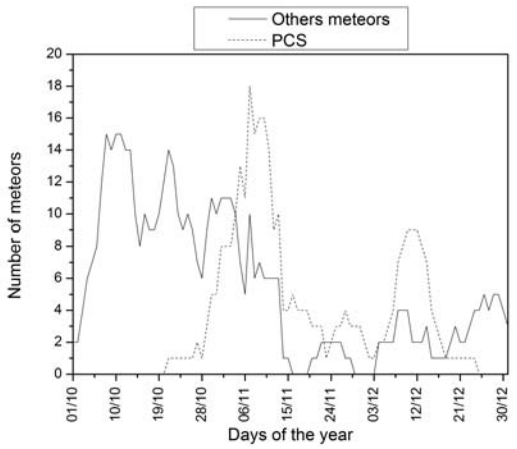

Figure 39 – PCS Valideitor, 20° radius ($D \leq 0.22$).

and that, as detailed in the NEC radiant, these other radiants seem to be orbitally distant from the PCS.

Figure 40 is a stream representation of the PCS radiant meteors. This representation was created by exporting the orbital data of 71 meteor belonging to PCS (with $D \leq 0.1$).

A search for parent bodies of the PCS radiant has returned several possible candidates. The four candidates with the most similar orbits the asteroids 2009 WX$_7$, 2010 VW$_{194}$, 2014 WX$_4$, and 2015 XM$_{169}$, respectively. 2009 WX$_7$ is the potential parent body with the highest orbital similarity ($D = 0.0135$).

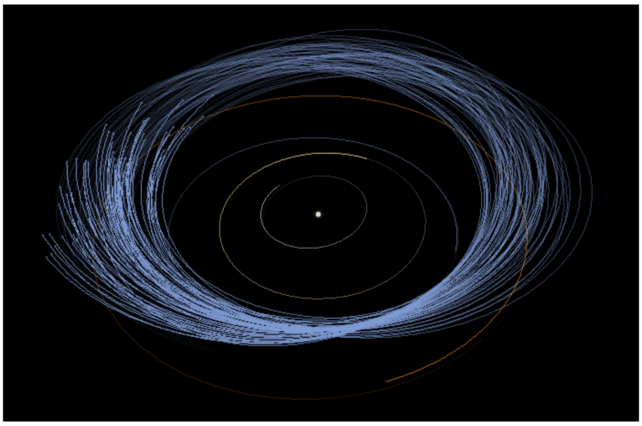

Figure 40 – Stream representation of the PCS ($D \leq 0.1$).

3.11 USG – Phi Ophiuchids

Figure 41 shows the orbit distribution of the USG radiant, and we can notice the radiant coverage area (right ascension from $\approx 210°$ to $\approx 290°$ and declination from $\approx -22°$ to $\approx -2\overset{\circ}{.}5$). We can also notice that the speed of the meteors seems to increase as the right ascension decreases and the declination increases.

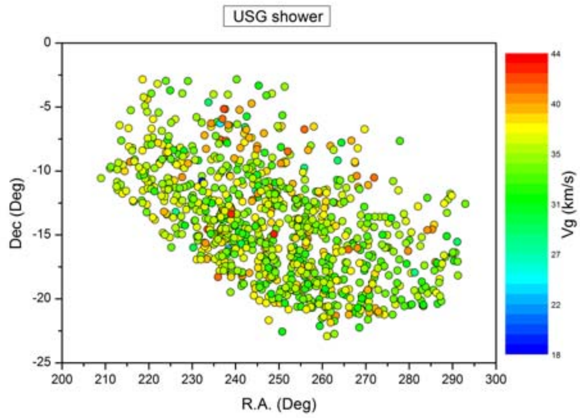

Figure 41 – Radiant of the Phi Ophiuchids (USG).

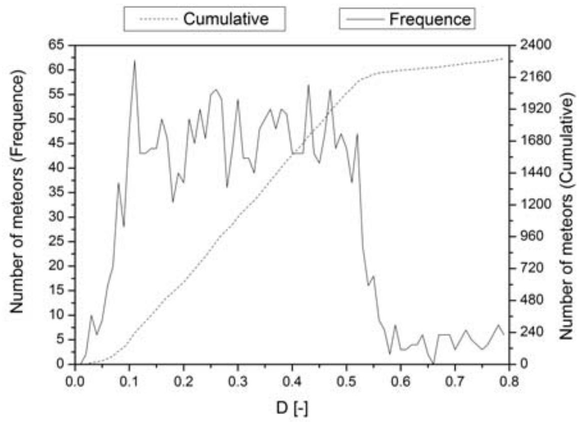

Figure 42 – USG Breakpoint+ plot with a 20 degree radius.

Figure 42 shows the USG breakpoint+ plot, whose inflection point occurs late, near $D = 0.5$, i.e., the orbits associated to the radiant are not concentrated relative to the radiant's mean orbit.

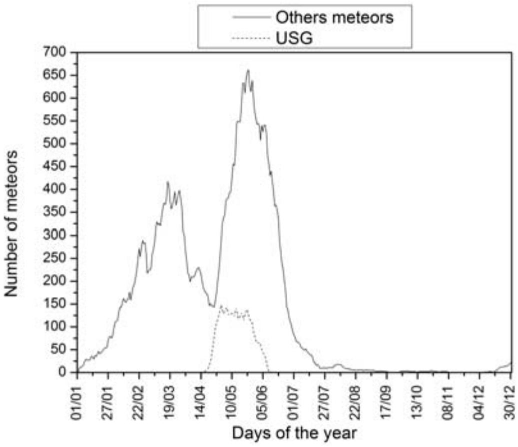

Figure 43 – USG Valideitor, 20° radius ($D \leq 0.22$).

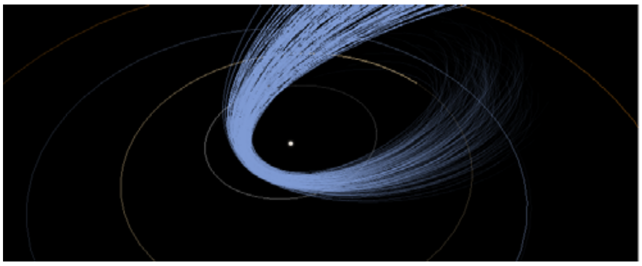

Figure 44 – Stream representation of the USG ($D \leq 0.1$).

Figure 43 presents the Valideitor plot, which shows radiant activity between April and June. We can also notice the activity of other radiants along with the USG radiant, and it is likely that there is a relationship between USG and other nearby radiants.

Figure 44 is a stream representation of the USG radiant meteors. This representation was created by exporting the orbital data of 195 meteors belonging to USG (with $D \leq 0.1$).

3.12 XCD – October Cetids

Figure 45 shows the orbit distribution of the XCD radiant, and we can notice the radiant coverage area (right ascension from ≈ 30° to ≈ 75° and declination from ≈ +2.°5 to ≈ +22°). We can also notice that the speed of the meteors seems to increase as the right ascension decreases and the declination increases.

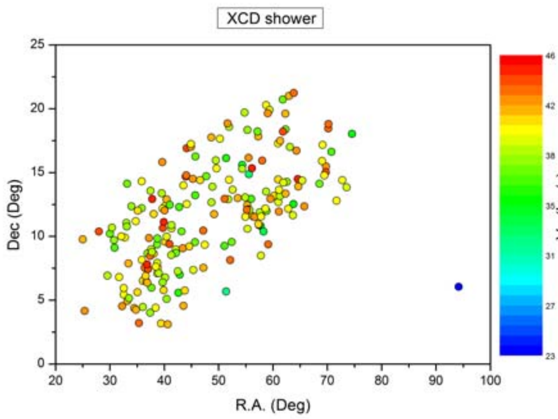

Figure 45 – Radiant of the October Cetids (XCD).

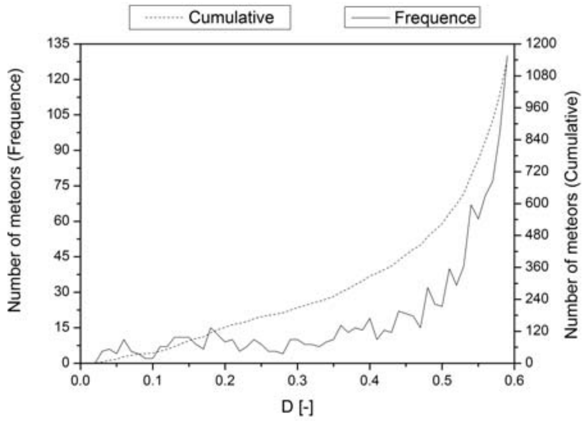

Figure 46 – XCD Breakpoint+ plot with a 20 degree radius.

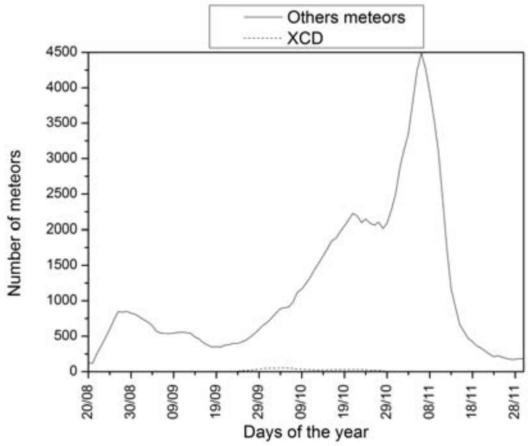

Figure 47 – XCD Valideitor, 20° radius ($D \leq 0.22$).

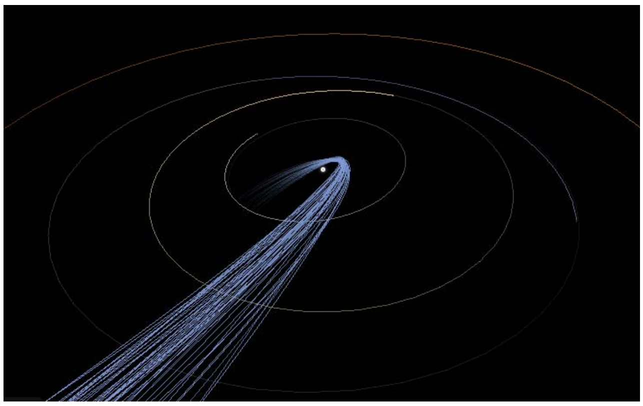

Figure 48 – Stream representation of the XCD ($D \leq 0.1$).

Figure 46 shows the XCD breakpoint+ plot, and we can observe two small inflection points on the plot (close to 0.07 and 0.25). We can also notice that after $D > 0.5$ the plot grows rapidly. This indicates that the XCD radiant became orbitally "close" at this point to a much larger radiant, which is clear when we look at the Valideitor plot in Figure 47. In this plot, the radiant shows modest activity when compared to other radiants occurring at the same location, i.e., XCD is hard to detect (specially through visual methods) since it is a small radiant occurring at the location of activity of much larger radiants. The Breakpoint+ plot shows a relationship between XCD and other nearby radiants, however, it is important to notice that the orbits associated with the XCD are distant from orbits of other known radiants.

Figure 48 is a stream representation of the XCD radiant meteors. This representation was created by exporting the orbital data of 46 meteors belonging to XCD (with $D \leq 0.1$).

3.13 LCP – Lambda Capricornids

Figure 49 shows the distribution of orbits associated with the LCP radiant. We find a radiant coverage area in right ascension from ≈ 300° to ≈ 50° and in declination from ≈ −50° to ≈ +15°. We can also notice that the speed of the meteors seems to increase as the right ascension decreases and the declination increases.

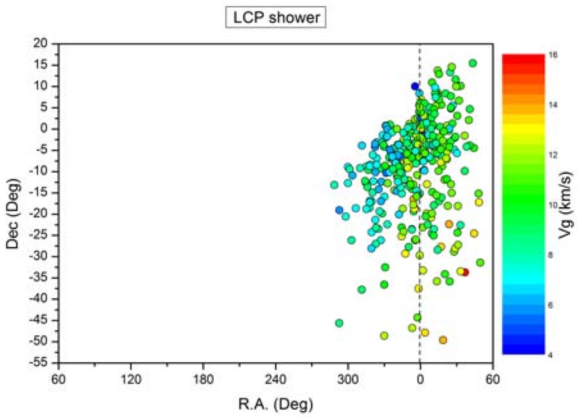

Figure 49 – Radiant of the Lambda Capricornids (LCP).

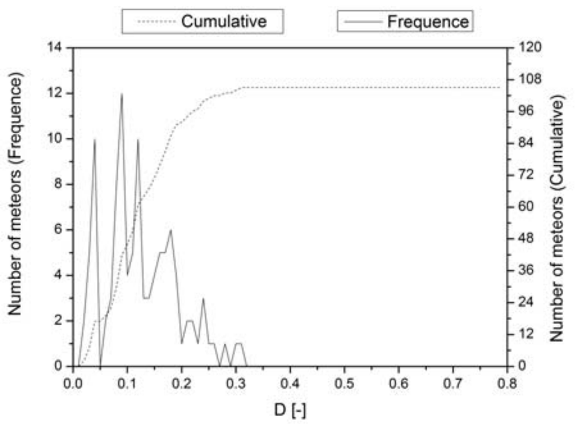

Figure 50 – LCP Breakpoint+ plot with a 20 degree radius.

Figure 50 shows the LCP breakpoint+ plot, whose inflection point occurs early, close to $D = 0.2$, i.e., despite being a radiant with very few orbits recorded, they are well concentrated relative to the mean orbit belonging to the radiant.

Figure 51 shows the Valideitor plot, in which we can identify the radiant's activity between the end of September and the beginning of November. Some peaks show a higher occurrence of meteors among radiants being active in the same period. Additionally, we can notice the activity from other radiants occurring together with the LCP shower. Such radiants appear to be distant in terms of their orbits, just as explained in detail for the NEC radiant.

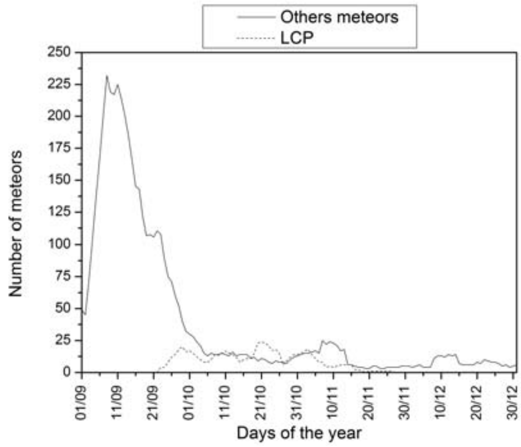

Figure 51 – LCP Valideitor, 20° radius ($D \leq 0.22$).

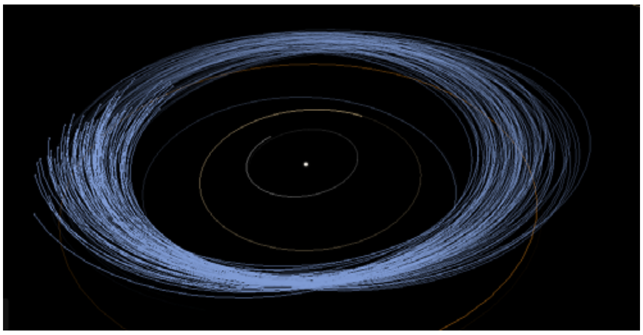

Figure 52 – Stream representation of the LCP ($D \leq 0.1$).

Figure 52 is a stream representation of the meteors related to the LCP radiant. This representation was created by exporting the orbital data of 96 meteors belonging to LCP (with $D \leq 0.1$).

A search for parent bodies of the LCP radiant has returned several possible candidates. The two candidates with the most similar orbits are 2014 RQ_{17}, and 2016 TD_{11}, and 2014 RQ_{17} is the parent body with the highest orbital similarity ($D = 0.0257$).

3.14 NAA – November alpha Aurigids

Figure 53 shows the orbit distribution of the NAA radiant, and we can notice the radiant coverage area (right ascension from ≈ 40° to ≈ 125° and declination from ≈ +38° to ≈ +54°). We can also notice that the

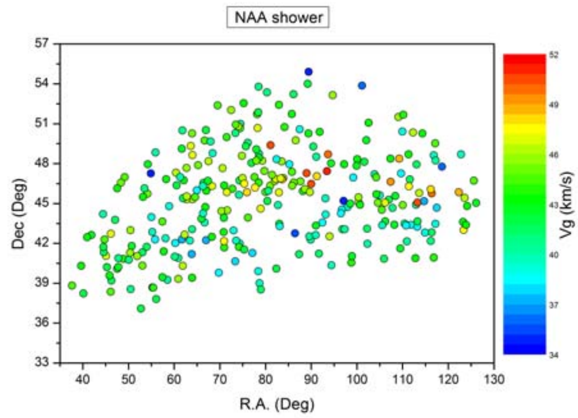

Figure 53 – Radiant of the November alpha Aurigids (NAA).

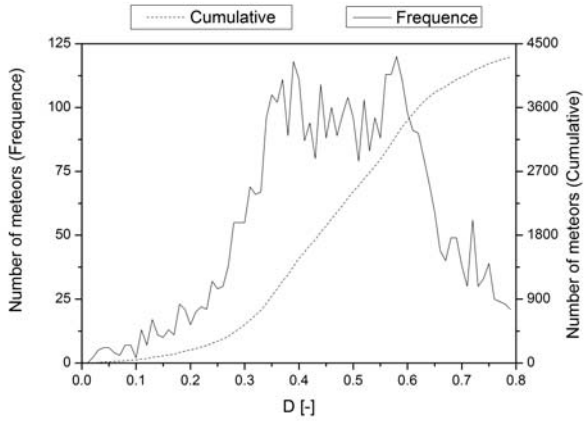

Figure 54 – NAA Breakpoint+ plot with a 20 degree radius.

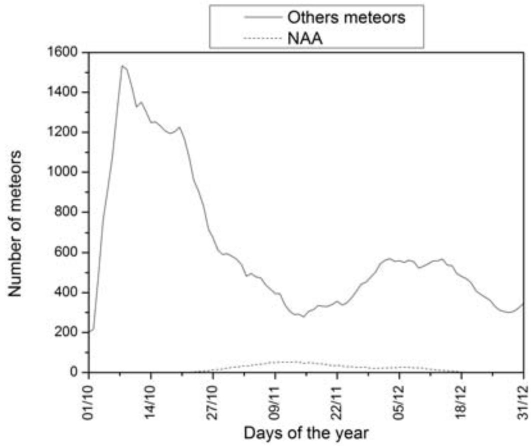

Figure 55 – NAA Valideitor, 20° radius ($D \leq 0.22$).

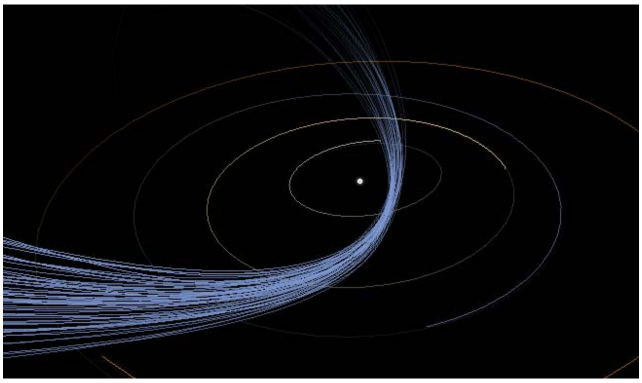

Figure 56 – Stream representation of the NAA ($D \leq 0.1$).

speed of the meteors seems to increase as the declination increases.

Figure 54 shows the NAA breakpoint+ plot, whose inflection point occurs late, close to $D = 0.6$, i.e., the radiant's orbits are not concentrated in relation to the radiant's mean orbit.

Figure 55 presents the Valideitor plot, which shows the radiant activity occurring between October and December. We can also notice the strong activity of other radiants occurring together with the NAA radiant.

Figure 56 is a stream representation of the NAA radiant meteors. This representation was created by exporting the orbital data of 61 meteors belonging to the NAA (with $D \leq 0.1$).

3.15 OAC – October alpha Camelopardalids

Figure 57 shows the orbit distribution of the OAC radiant, in which we can see the radiant coverage area (right ascension from $\approx 340°$ to $\approx 50°$ and declination from $\approx -30°$ to $\approx +20°$). We can also notice that the speed of the meteors seems to increase as thew right ascension decreases and the declination increases.

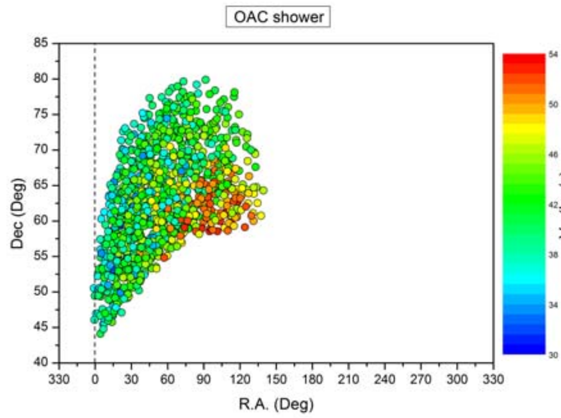

Figure 57 – Radiant of the October alpha Camelopardalids (OAC).

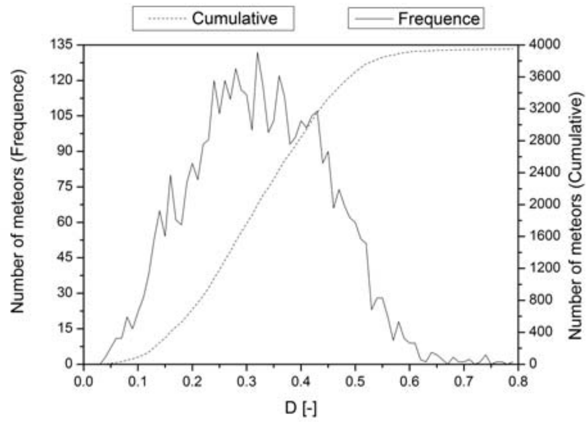

Figure 58 – OAC Breakpoint+ plot with a 20 degree radius.

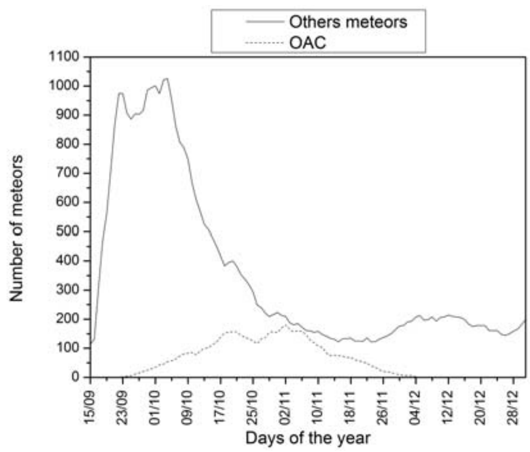

Figure 59 – OAC Valideitor, 20° radius ($D \leq 0.22$).

Figure 58 shows the OAC breakpoint+ plot, whose inflection point occurs early, near $D = 0.5$, i.e., the

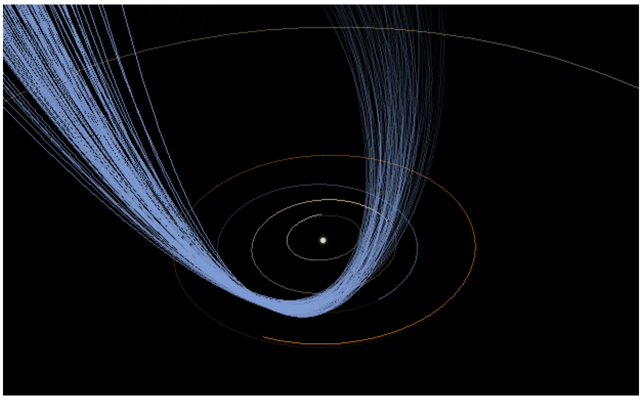

Figure 60 – Stream representation of the OAC ($D \leq 0.1$).

radiant's orbits are not concentrated relative to the radiant's mean orbit.

Figure 59 presents the Valideitor plot, which shows that the radiant's activity occurs between September and December. We can also notice the activity of other radiants together with the OAC radiant. The OAC is likely related to nearby radiants.

Figure 60 is a stream's representation of the OAC radiant meteors. This representation was created by exporting the orbital data of 103 meteors belonging to OAC (with $D \leq 0.1$).

3.16 CVD – January Canum Venaticids

Figure 61 shows the orbit distribution of the CVD radiant. The radiant coverage extends over an area between $\approx 0°$ and $\approx 140°$ in right ascension and from $\approx +44°$ to $\approx +80°$ in declination. We can also notice that the speed of the meteors seems to increase as the right ascension decreases and the declination increases.

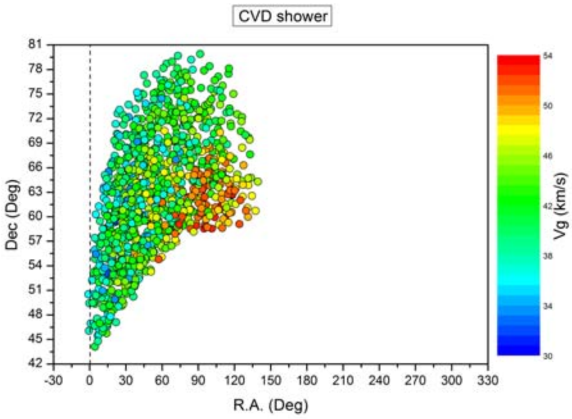

Figure 61 – Radiant of the January Canum Venaticids (CVD).

Figure 62 presents the CVD breakpoint+ plot, whose inflection point occurs late, close to $D = 0.5$. We can also notice that after $D > 0.4$ the plot grows rapidly, indicating that at this point the orbits of meteors associated to the CVD radiant were "close" to those of another radiant. This generated a rapid increase in the number of meteors in the plot at this position. This is evident when we look at the Valideitor plot in Figure 63, in which the radiant's activity is accompanied by strong activity from other radiants occurring at the same position. Some of these radiants may be orbitally related with the CVD.

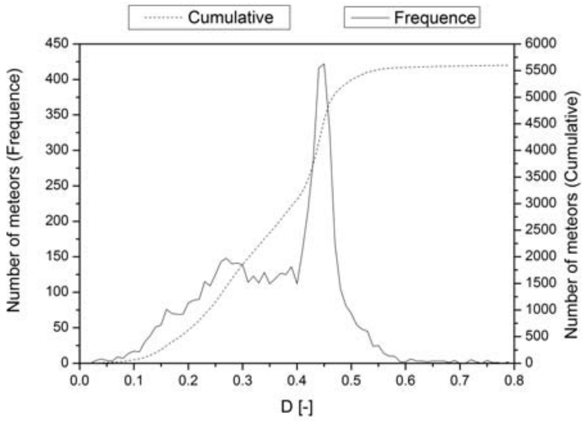

Figure 62 – CVD Breakpoint+ plot with a 20 degree radius.

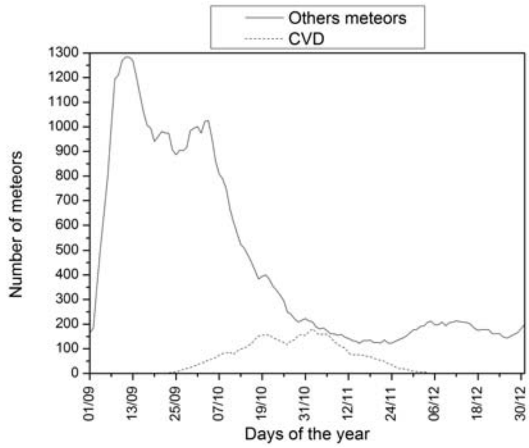

Figure 63 – CVD Valideitor, 20° radius ($D \leq 0.22$).

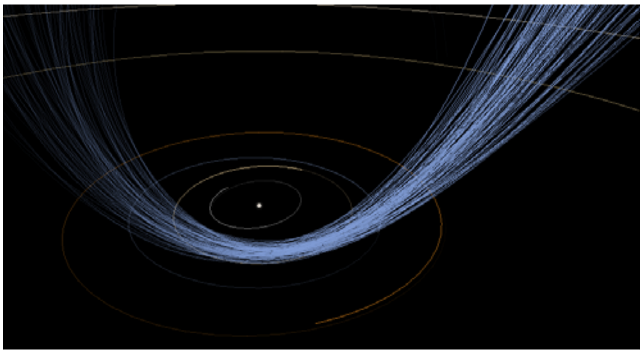

Figure 64 – Stream representation of the CVD ($D \leq 0.1$).

Figure 64 is a stream representation of the CVD radiant meteors. This representation was created by exporting the orbital data of 103 meteors belonging to CVD (with $D \leq 0.1$).

3.17 UMS – August Ursae Majorids

Figure 65 shows the orbit distribution of the UMS radiant, and we can notice the radiant coverage area (right ascension from $\approx 60°$ to $\approx 210°$ and declination from $\approx +45°$ to $\approx +85°$). We can notice that two regions of meteor occurrence are formed. UMS gives rise to the concentration of orbits with positive declination and another radiant (not yet published) gives rise to the concentration of orbits on the left, and these two radi-

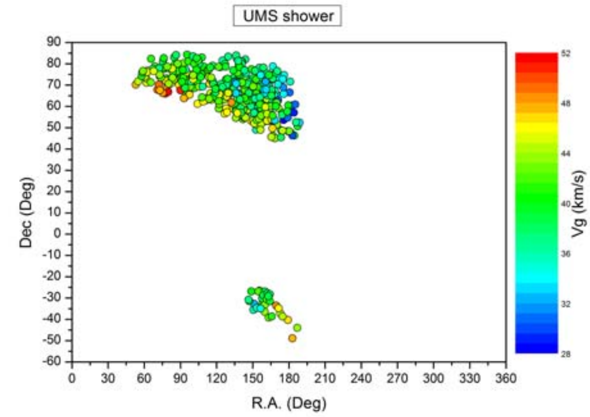

Figure 65 – Radiant of the August Ursae Majorids (UMS).

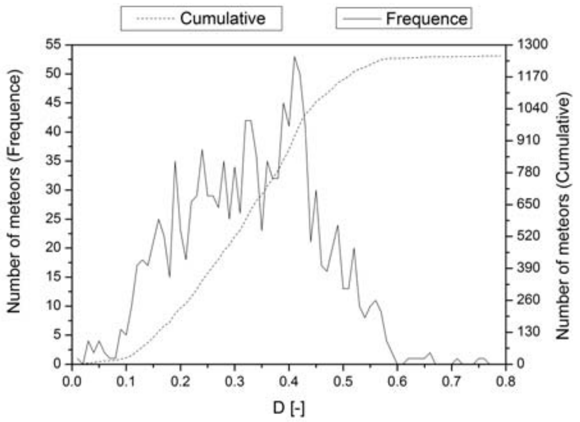

Figure 66 – UMS Breakpoint+ plot with a 20 degree radius.

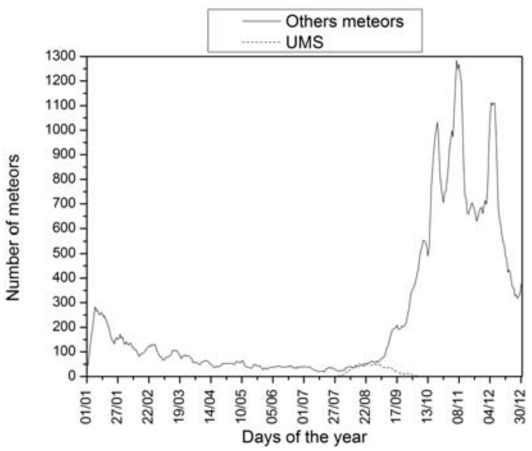

Figure 67 – UMS Valideitor, 20° radius ($D \leq 0.22$).

ant may be related and share a common parent body. We can also notice that the speed of the meteors seems to increase as the right ascension decreases and the declination increases.

Figure 66 shows the UMS breakpoint+ plot, whose inflection point occurs late, near $D = 0.55$, i.e., the radiant's orbits are not concentrated in relation to the radiant's mean orbit.

Figure 67 presents the Valideitor plot, which shows that the radiant's activity occurs between September and December. We see activity from other radiants together with the UMS radiant. The UMS is likely related to nearby radiants.

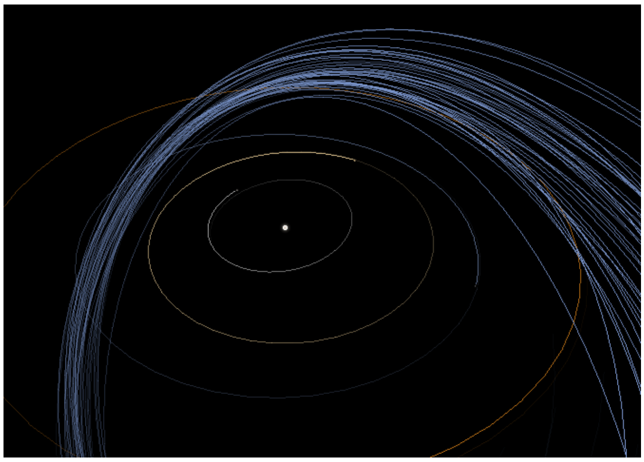

Figure 68 – Stream representation of the UMS ($D \leq 0.1$).

Figure 68 is a stream representation of the UMS radiant meteors. This representation was created by exporting the orbital data of 42 meteors belonging to UMS (with $D \leq 0.1$).

3.18 CVT – February Canum Venaticids

Figure 69 shows the orbit distribution of the CVT radiant, and we can notice the radiant coverage area (right ascension from $\approx 150°$ to $\approx 230°$ and declination from $\approx +22°$ to $\approx +55°$). We can also notice that the speed of the meteors seems to increase as the right ascension increases and the declination decreases.

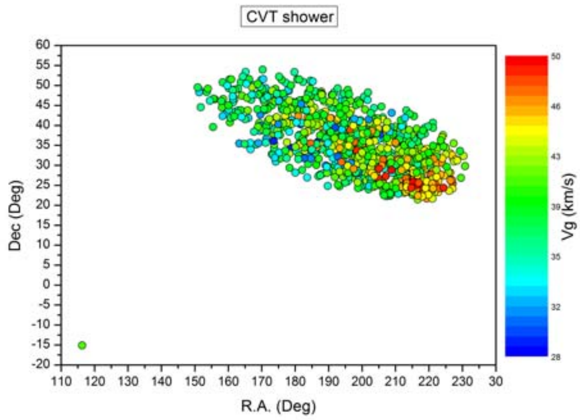

Figure 69 – Radiant of the February Canum Venaticids CVT).

Figure 70 shows the CVT breakpoint+ plot, whose inflection point occurs late, near $D = 0.6$, i.e., the radiant's orbits are not concentrated in relation to the radiant's mean orbit.

Figure 71 presents the Valideitor plot, which shows radiant activity between January and March. We can also notice the activity of other radiants occurring together with the CVT radiant. The CVT is likely related to nearby radiants.

Figure 72 is a stream representation of the CVT radiant meteors. This representation was created by exporting the orbital data of 125 meteors belonging to the CVT (with $D \leq 0.1$).

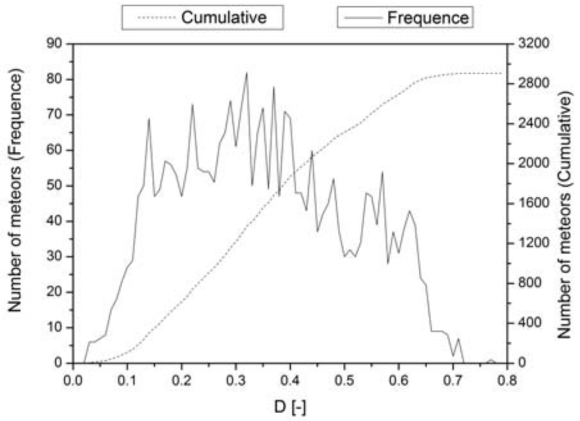

Figure 70 – CVT Breakpoint+ plot with a 20 degree radius.

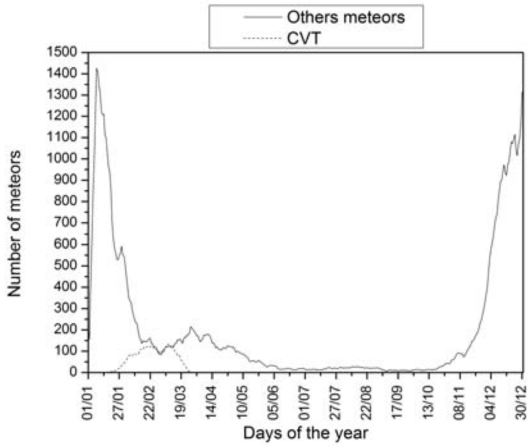

Figure 71 – CVT Valideitor, 20° radius ($D \leq 0.22$).

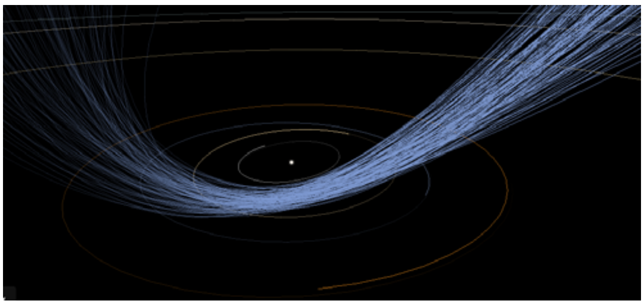

Figure 72 – Stream representation of the CVT ($D \leq 0.1$).

3.19 PCI – 42 Piscids

Figure 73 shows the orbit distribution of the PCI radiant. We can notice the radiant coverage area (right ascension from ≈ 330 to ≈ 60° and declination from ≈ −5° to ≈ +35°). We can also notice that the speed of the meteors seems to increase as the right ascension decreases and the declination increases.

Figure 74 shows the PCI breakpoint+ plot, whose inflection point occurs early, near $D = 0.4$, i.e., the radiant's orbits are weakly concentrated in relation to the radiant's mean orbit.

Figure 75 presents the Valideitor plot. In the plot we can identify the activity of the radiant between July and September. We can also notice the activity of other radiants occurring together with the PCI radiant. PCI is likely to be related to these radiants.

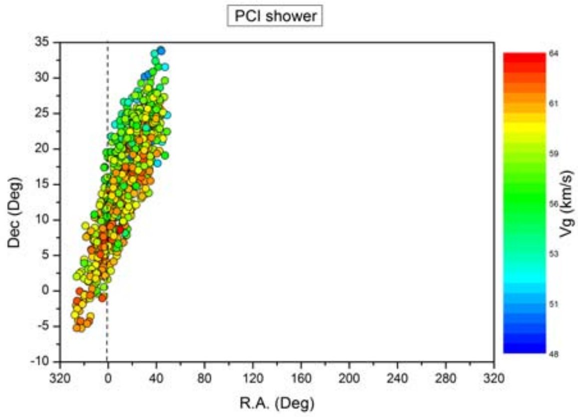

Figure 73 – Radiant of the 42 Piscids (PCI).

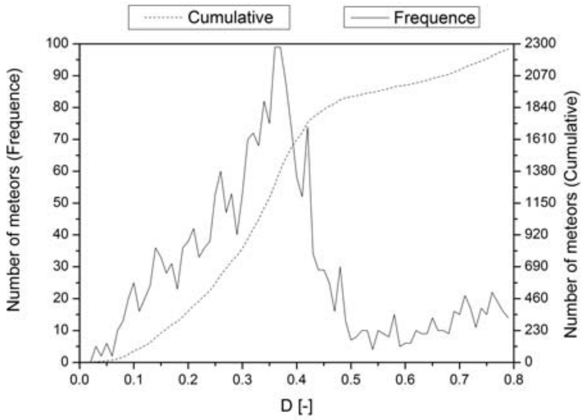

Figure 74 – PCI Breakpoint+ plot with a 20 degree radius.

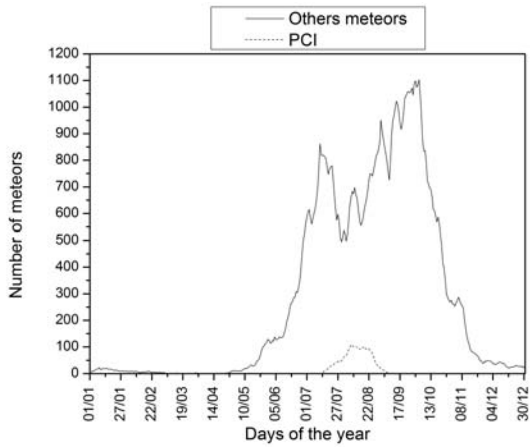

Figure 75 – PCI Valideitor, 20° radius ($D \leq 0.22$).

Figure 76 is a stream representation of the meteors forming the PCI radiant. This representation was created by exporting the orbital data of 100 meteors belonging to the PCI (with $D \leq 0.1$).

3.20 OAG – October Aurigids

Figure 77 shows the orbit distribution of the OAG radiant. We can notice the radiant coverage area (right ascension from ≈ 30° to ≈ 110° and declination from ≈ +24° to ≈ +43°). We can also notice that the speed of the meteors seems to increase as the right ascension decreases and the declination increases.

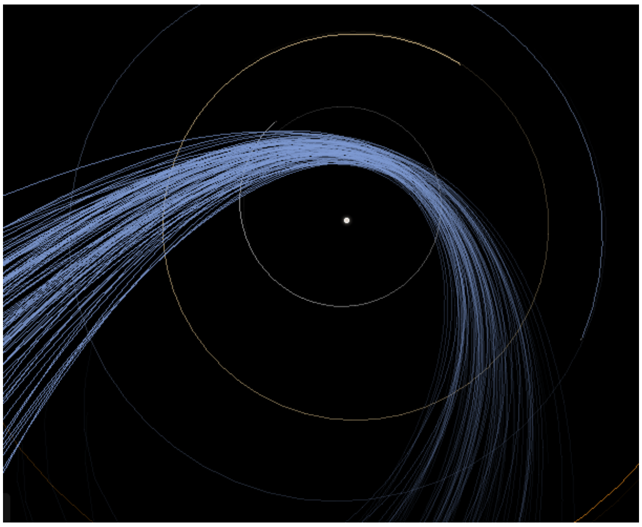

Figure 76 – Stream representation of the PCI ($D \leq 0.1$).

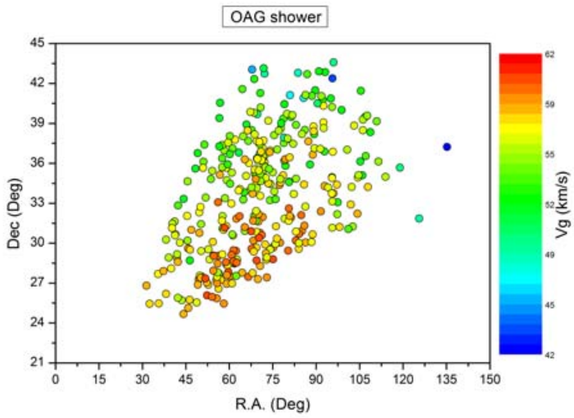

Figure 77 – Radiant of the October Aurigids (OAG).

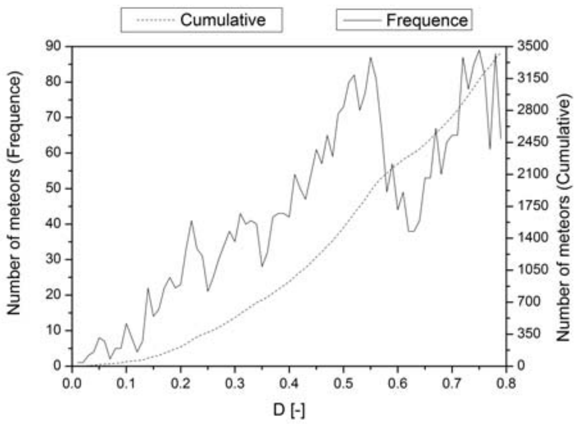

Figure 78 – OAG Breakpoint+ plot with a 20 degree radius.

Figure 78 shows the OAG breakpoint+ plot, whose inflection point occurs early, near $D = 0.55$, i.e., the radiant's orbits are not concentrated towards the radiant's mean orbit.

Figure 79 presents the Valideitor plot. In the plot we can identify the formation of a maximum activity peak in the radiant near the end of October and beginning of November. We can also notice the activity of other radiants occurring together with the OAG radiant. The OAG is likely related to nearby radiants.

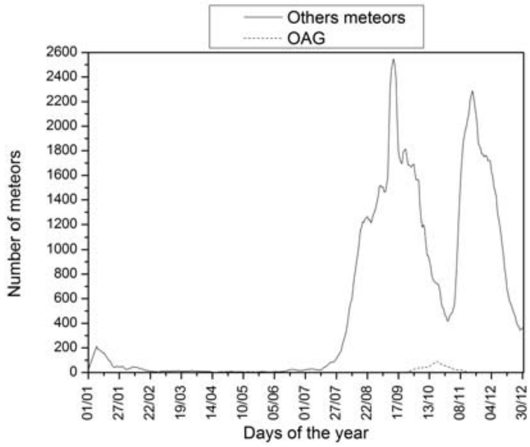

Figure 79 – OAG Valideitor, 20° radius ($D \leq 0.22$).

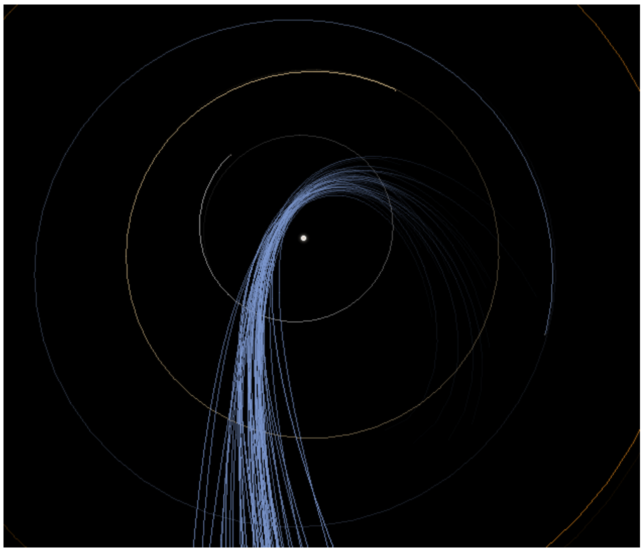

Figure 80 – Stream representation of the OAG ($D \leq 0.1$).

Between $\lambda_\odot = 191°$ and $209°$ there are seven more showers with radiants in or near Auriga in the IAU data base. If we compare the orbital parameters of the radiants, we see that all of them show a dissimilarity $D > 0.1$ implying that they are quite distant.

Figure 80 is a stream representation of the OAG radiant meteors. This representation was created by exporting the orbital data of 56 meteors belonging to the OAG (with $D \leq 0.1$).

3.21 SPS – Sigma Perseids

Figure 81 shows the orbit distribution of the SPS radiant. We can notice the radiant coverage area (right ascension from $\approx 0°$ to $\approx 105°$ and declination from $\approx +30°$ to $\approx +60°$). We can also notice that the speed of the meteors seems to increase as the right ascension decreases and the declination increases.

Figure 82 shows the SPS breakpoint+ plot, whose inflection point occurs early, near $D = 0.35$, i.e., the radiant's orbits are weakly concentrated in relation to the radiant's mean orbit.

Figure 83 presents the Valideitor plot. In the plot we can identify the formation of a maximum activity peak in the radiant near the beginning of September. The peak of September seems to be related to another much larger radiant (possibly SPE). After this peak, another

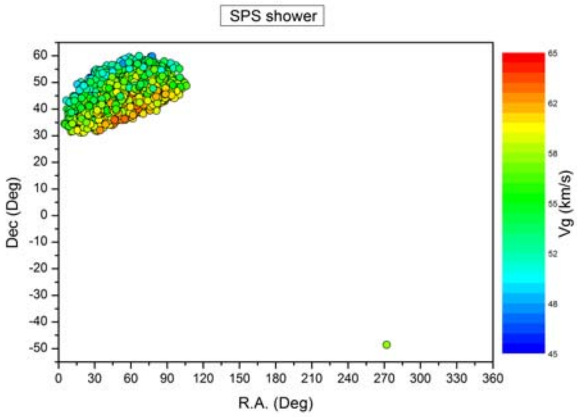

Figure 81 – Radiant of the Sigma Perseids (SPS).

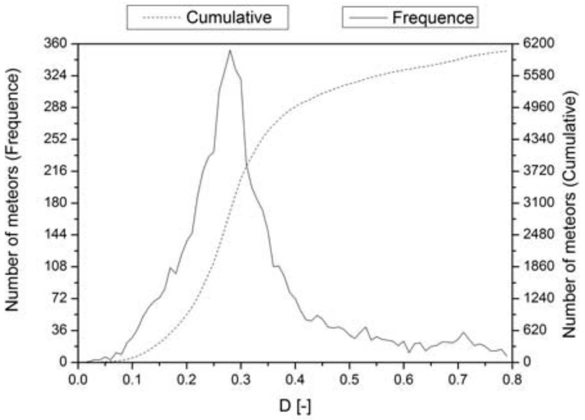

Figure 82 – SPS Breakpoint+ plot with a 20 degree radius.

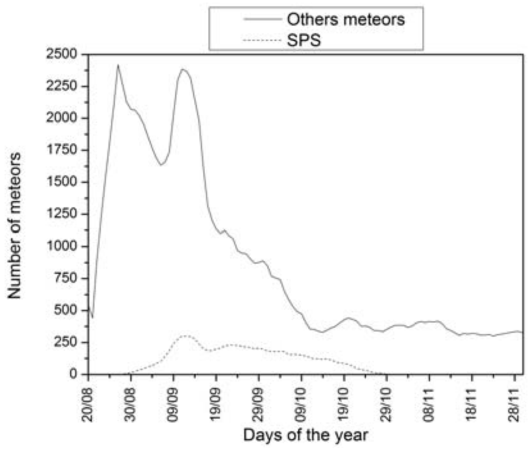

Figure 83 – SPS Valideitor, 20° radius ($D \leq 0.22$).

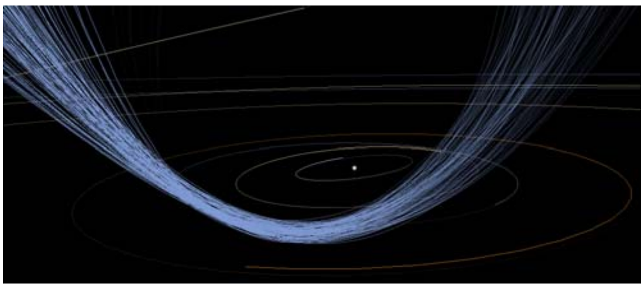

Figure 84 – Stream representation of the SPS ($D \leq 0.1$).

small peak occurs and then the radiant activity tends to decrease smoothly (while the activity of the other radiant decreases rapidly) extending until the end of October. SPS may be related to the SPE, and perhaps may be a stream that is drifting away.

Figure 84 is a stream representation of the SPS radiant meteors. This representation was created by exporting the orbital data of 110 meteors belonging to SPS (with $D \leq 0.1$).

3.22 TRD – October Taurids

Figure 85 shows the orbit distribution of the TRD radiant. We can notice the radiant coverage area (right ascension from $\approx 45°$ to $\approx 120°$ and declination from $\approx +0°$ to $\approx 25°$). We can also notice that the speed of the meteors seems to increase as the right ascension decreases and the declination increases.

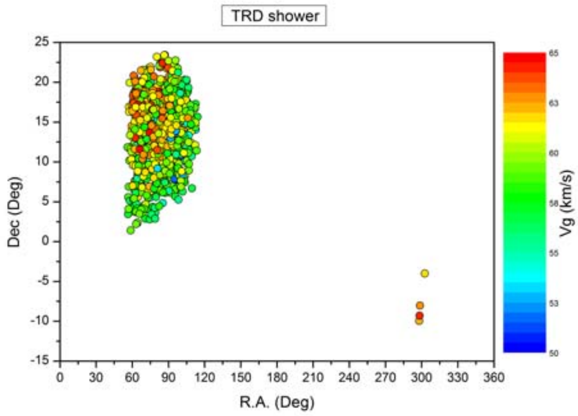

Figure 85 – Radiant of the October Taurids (TRD).

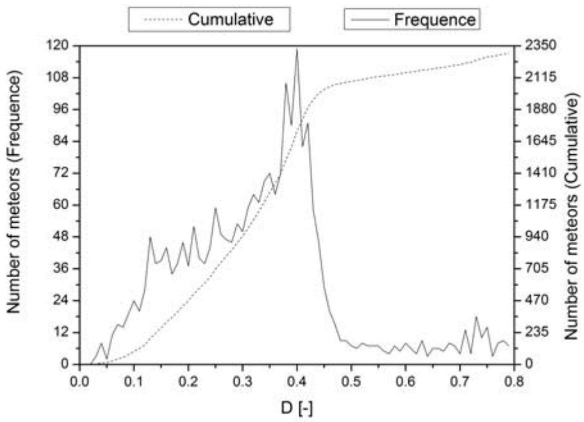

Figure 86 – TRD Breakpoint+ plot with a 20 degree radius.

Figure 86 shows the TRD breakpoint+ plot, whose inflection point occurs early, near $D = 0.4$, i.e., the radiant's orbits are weakly concentrated in relation to the radiant's mean orbit.

Figure 87 presents the Valideitor plot. In the plot we can identify the activity of the radiant between September and November. We can also notice the activity of other radiants occurring together with the TRD radiant.

Figure 88 is a stream representation of the TRD radiant meteors. This representation was created by

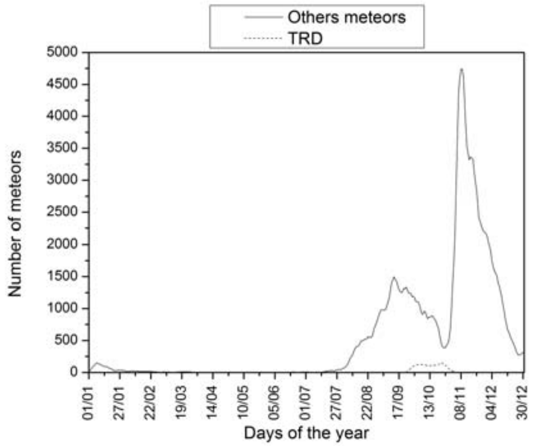

Figure 87 – TRD Valideitor, 20° radius ($D \leq 0.22$).

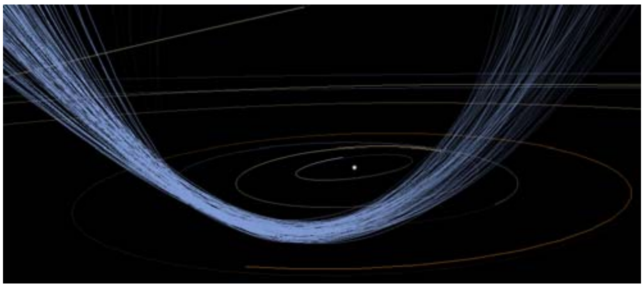

Figure 88 – Stream representation of the TRD ($D \leq 0.1$).

exporting the orbital data of 107 meteors belonging to TRD (with $D \leq 0.1$). We found $D > 0.108$ when comparing the TRD orbit with meteors of other Taurid radiants in the IAU list which are also active during the September – November period. The value of D indicates the TRD is different from the two branches of the known Taurids (017 NTA, 002 STA) and the other showers in the respective period.

3.23 DRP – December rho Puppids

Figure 89 shows the orbit distribution of the DRP radiant. We can notice the radiant coverage area (right ascension from $\approx 90°$ to $\approx 160°$ and declination from $\approx -40°$ to $\approx -10°$). We can also notice that the speed of the meteors seems to increase as the right ascension decreases and the declination increases.

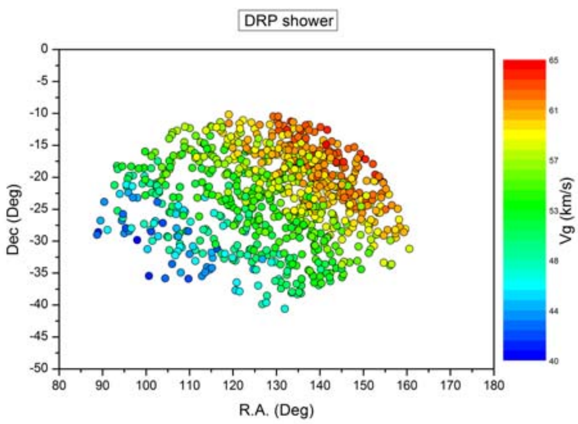

Figure 89 – Radiant of the December rho Puppids (DRP).

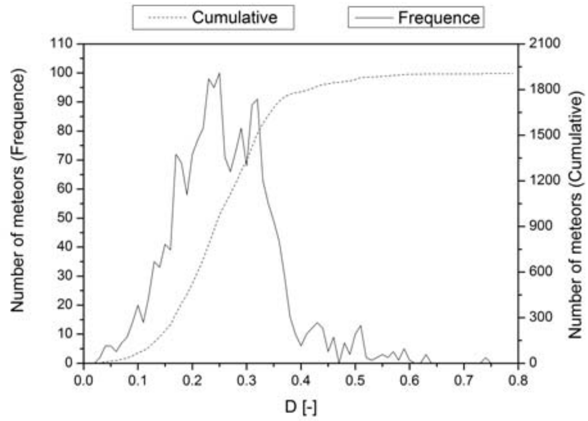

Figure 90 – DRP Breakpoint+ plot with a 20 degree radius.

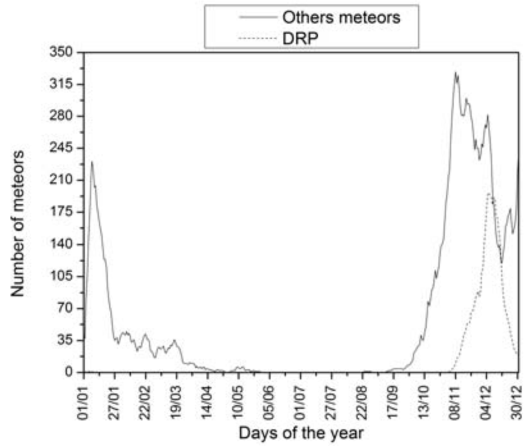

Figure 91 – DRP Valideitor, 20° radius ($D \leq 0.22$).

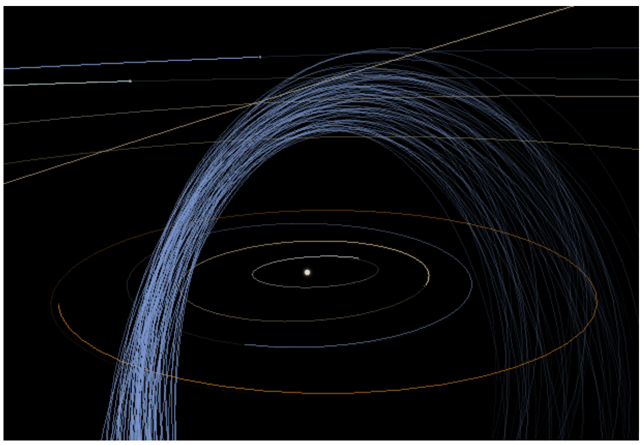

Figure 92 – Stream representation of the DRP ($D \leq 0.1$).

Figure 90 shows the DRP breakpoint+ plot. We can see that the inflection point occurs early, near $D = 0.3$, i.e., the radiant's orbits are weakly concentrated in relation to the radiant's mean orbit.

Figure 91 presents the Valideitor plot. In the plot we can identify the formation of a maximum activity peak in the radiant near the beginning of December. We can also notice the activity of other radiants occurring together with the DRP radiant.

Figure 92 is a stream representation of the DRP radiant meteors. This representation was created by exporting the orbital data of 110 meteors belonging to DRP (with $D \leq 0.1$).

3.24 Conclusion

Based on the method of Amaral et al. (2018a), in a short time the Encontreitor software, proved to be an efficient computational application for finding new radiants. The current meteor databases have already been thoroughly searched for new radiants. However, many small radiants are still camouflaged by the occurrence of other larger radiants. Such radiants are difficult to discover (especially if depending on visual analysis).

The capability of the method proposed by Amaral et al. (2018a) to search for radiants based on orbital similarities allowed BRAMON to find radiants which were "invisible" until now by other methods.

The method was also able to identify a number of twin radiants, such as ADS, DGR, GSC, and UMS.

Some radiants (ADS, LSA, FLO, XCD, NAA, CVD, UMS, CVT, and OAG) have been found later by other authors using other methods. This confirms the robustness of the radiants found by Encontreitor.

We were also able to identify parent bodies with orbital similarity very close to the mean orbit of the meteors associated to the radiants of the NEC, PCS, and PCL.

References

Amaral L., Di Pietro C., Trindade L., Zurita M., Silva G., Domingues M., Poltronieri R., Jacques C., and Jung C. (2018a). "A search method for meteor radiants". *WGN, Journal of the International Meteor Organization*, **46:6**, 191–197.

Amaral L., Trindade L., Di Pietro C., Zurita M., Poltronieri R., Silva G., Jacques C., Jung C., and Koukal J. (2018b). "Brazilian Meteor Observation Network: History of creation and first developments". In *Proceedings of the International Meteor Conference, Petnica, Serbia, September 21–24 2017*. IMO, pages 171–175.

Drummond J. D. (1981). "A test of comet and meteor shower associations". *Icarus*, **45:3**, 545–553.

EDMOND (2018). "EDMOND Database". `https://fmph.uniba.sk/en/microsites/daa/division-of-astronomy-and-astrophysics/research/meteors/edmond/`.

Galligan D. P. (2001). "Performance of the D-criteria in recovery of meteoroid stream orbits in a radar data set". *MNRAS*, **327**, 623–628.

Jopek T. J., Valsecchi G. B., and Froeschlé C. (2002). "Asteroid meteoroid streams". In Bottke, Jr. W. F., Cellino A., Paolicchi P., and Binzel R. P., editors, *Asteroids III, first edition*, pages 645–652. University of Arizona Press, Tucson.

Kornoš L., Koukal J., Piffl R., and Tóth J. (2014a). "EDMOND Meteor Database". In Gyssens M., Roggemans P., and Zoladek P., editors, *Proceedings of the International Meteor Conference, Poznán, Poland, Aug. 22-25, 2013*. IMO, pages 23–25.

Kornoš L., Matlovič P., Rudawska R., Tóth J., Hajduková, Jr. M., Koukal J., and Piffl R. (2014b). "Confirmation and characterization of IAU temporary meteor showers in EDMOND database". In Jopek T. J., Rietmeijer F. J. M., Watanabe J., and Williams I. P., editors, *Proceedings of the Meteoroids 2013 Conference, A.M. University, Poznán, Poland, Aug. 26-30, 2013*. pages 225–233.

SonotaCo (2009). "A meteor shower catalog based on video observations in 2007–2008". *WGN, Journal of the IMO*, **37**, 55–62.

SonotaCo (2018). "SonotaCo Network Simultaneously Observed Meteor Data Sets". `http://sonotaco.jp/doc/SNM/`.

Trindade L., Zurita M., Silva G., Daláva A., and Di Pietro C. (2019). "Identification of two new meteor showers: #797 EGR and #798 ACD". *WGN, Journal of the IMO*, **47:6**, 184–187.

Universe Sandbox (2020). "Universe Sandbox 2.2". `http://universesandbox.com/`.

Handling Editor: Jürgen Rendtel